

---

# **Structural Changes in Cylinder-Forming PS-*b*-PB Thin Films During Solvent Vapor Annealing**

---

**by Tim Birger Tejsner**

Supervisor: Dorthe Posselt

MASTER THESIS IN PHYSICS  
SEPTEMBER 30, 2015  
ROSKILDE UNIVERSITET



## Abstract

The orientational changes of cylinders in Polystyrene-*b*-Polybutadiene (PS-*b*-PB) diblock copolymer thin films during solvent vapor annealing (SVA) was investigated using White-Light Interferometry (WLI) and time-resolved grazing-incidence small-angle x-ray scattering (GISAXS). The SVA procedure was performed with three different solvents of varying selectivity to the two blocks: Ethyl Acetate (EAC), Toluene (TOL) and Cyclohexane (CHX). A change from standing to lying cylinders was found using all three solvents. The orientational change appears to depend on the minimal polymer volume fraction  $\phi_{\min}$  of the film, and different threshold values were found for each solvent:  $\phi_{\min,EAC} = 0.66$ ,  $\phi_{\min,TOL} = 0.63$ ,  $\phi_{\min,CHX} = 0.49$ . In one experiment with CHX, the switch from standing to lying cylinders happens through a disordered phase spanning 15 minutes. This, along with other circumstantial evidence, hints at the timescales of structural changes.



## Acknowledgements

First of all, I would like to thank my supervisor Dorthe Posselt for her consistent help and guidance throughout the entire process.

Second, I would like to thank the people at CHESS. The administration and, in particular, our beamline scientist Detlef-M. Smilgies were instrumental in making the experiments a smooth and pleasant experience. In the same breath, I would like to thank Florian Jung and Anatoly V. Berezkin from Technische Universität München for their cooperation at the CHESS facility.

Lastly, I would like to thank my student secretary, Tine Nyegaard Pedersen. Her good spirits and helpful nature has made my MSc at Roskilde University a pleasant experience.



# Contents

<b>1</b>	<b>Introduction</b>	<b>7</b>
1.1	Structure of the thesis . . . . .	8
<b>2</b>	<b>Theory</b>	<b>9</b>
2.1	Diblock copolymer thermodynamics . . . . .	9
2.2	Scattering theory . . . . .	12
2.3	Cylinder models . . . . .	20
2.4	X-ray reflectivity . . . . .	25
<b>3</b>	<b>Experiment</b>	<b>29</b>
3.1	Materials . . . . .	29
3.2	Sample preparation . . . . .	30
3.3	Solvent vapor annealing . . . . .	30
3.4	Thickness measurements . . . . .	30
3.5	GISAXS . . . . .	31
<b>4</b>	<b>Results</b>	<b>33</b>
4.1	Procedure . . . . .	33
4.2	List of experiments . . . . .	39
4.3	Cyclohexane . . . . .	40
4.4	Ethyl acetate . . . . .	42
4.5	Toluene . . . . .	44
4.6	2015 . . . . .	44
<b>5</b>	<b>Discussion</b>	<b>47</b>
5.1	General observations . . . . .	47
5.2	Inhomogeneity . . . . .	48
5.3	GISAXS modelling . . . . .	48
5.4	X-ray reflectivity . . . . .	50
5.5	Data reduction . . . . .	50
5.6	Relevant results from literature . . . . .	51
<b>6</b>	<b>Conclusion</b>	<b>53</b>
	<b>Bibliography</b>	<b>65</b>



# 1 Introduction

Block copolymers are a class of materials consisting of different linear polymer chains (blocks) linked together by a covalent bond. Due to advances in synthetic methods, a rich variety of precisely manufactured block copolymers are available[3]. By varying the length of the polymer chains and the molecular constituents, block copolymers are equipped with rich phase behaviour that has attracted a lot of attention in recent years.

Due to the chemical incompatibility of the different polymer chains, block copolymers can separate locally and self-assemble into a wide variety of structures on length scales from a few nanometers to several micrometers.

By confining a block copolymer to a thin film, structures tend to form with an orientation relative to the surface. Directing the self-assembly of block copolymers in thin films are of great interest for a number of applications such as microelectronics, separation membranes, nanofluidics, photonics and biological scaffolds[36].

In the present work, an asymmetric Polystyrene-*b*-Polybutadiene (PS-*b*-PB) diblock copolymer thin film is investigated. *Asymmetric* refers to the fact that the polymer chains differ in length, and *diblock* indicates that it is composed of two polymer chains. Due to this asymmetry, this system tends to self-assemble into cylindrical Polystyrene microdomains embedded in a Polybutadiene matrix.

Due to the preparation methods of block copolymer films, the samples are usually equipped with a defect-rich morphology. In order to combat these defects and improve long-range order, a method known as solvent vapor annealing (SVA)[36] has been gaining momentum. By exposing the sample to a solvent atmosphere and subsequent drying, the resulting film structure can be controlled to varying degree.

This thesis is an attempt to characterize the dynamics of the polymer during SVA by an investigation of structural changes. Through a series of experiments performed from 2012-2015, SVA of PS-*b*-PB thin films have been investigated using three solvents of varying selectivity. The analysis of the data from these experiments constitute the bulk of the work performed in this thesis.

In order to characterize the structure of thin films, a method known *Grazing-Incidence Small Angle X-ray Scattering* (GISAXS) was used. By illuminating the sample with X-rays at grazing angles, the beam is reflected and give rise to interference patterns due to the film structure. The primary advantage of using GISAXS for structural determination is the fact that it can be used *in-situ*. The experiment is set up so that GISAXS data is collected roughly every 10 seconds while the SVA procedure is running.

However, the GISAXS method comes with a few caveats. Due to the low intensity of the scattered X-rays, experiments has to be performed at a synchrotron. The data contained in this thesis was collected at the CHESS facility at Cornell University[9]. Furthermore, GISAXS data is notoriously difficult to work with – in many cases only qualitative characterization can be extracted.

As the experiments contained in this work contain thousands of GISAXS intensity patterns, some amount of automated data-reduction must be performed in order to compare

experimental parameters and system dynamics. Part of the purpose of this thesis is to demonstrate how such data-reduction can be performed in a systematic way.

### 1.1 Structure of the thesis

Chapter 2 contains some of the fundamentals required to understand polymer thermodynamics and the GISAXS experiment. Chapter 3 describes the details of the experiments performed at CHESS. Chapter 4 is a presentation of the results from these experiments and a thorough description of the choices made in the data reduction. Chapter 5 is a discussion of the methodology, the obtained results and a comparison to relevant experiments in literature.

## 2 Theory

In this chapter, fundamentals relevant to the diblock copolymer thin film experiments will be presented. This includes an introduction to the thermodynamics of diblock copolymers and an overview of the GISAXS scattering technique. To illustrate the modelling aspect of GISAXS, a couple of examples from cylinder systems are investigated. Finally, some theoretical and practical aspects of X-ray reflectivity experiments are presented.

### 2.1 Diblock copolymer thermodynamics

Polymers are macromolecules composed of several identical molecular units linked together by covalent bonds. By linking two chemically distinct polymer chains (A and B) together a block copolymer is formed. Block copolymers come in several architectures depending on how the polymers are linked. The simplest configuration is the (A-B) diblock copolymer (DBCP), where the two blocks are linked together as shown in Figure 2.1. For the purposes of this thesis, only DBCPs in the amorphous state are considered (also known as a *polymer melt*).

DBCPs in bulk are mainly characterized by three parameters[2]. The overall degree of polymerization  $N$  is given by the total number of monomer units  $N_A + N_B$ . The composition

$$f_A = \frac{V_A}{V}$$

represents the volume fraction of the A-block. Lastly, the dimensionless Flory-Huggins parameter  $\chi$  describes the incompatibility between the two blocks due to the enthalpic and entropic effects. The first two parameters  $N$  and  $f_A$  are regulated in the polymerization process, while  $\chi$  depends on the chemical composition of the polymers. For the materials considered here, the Flory-Huggins parameter  $\chi$  has a temperature dependence[2]

$$\chi \approx \alpha T^{-1} + \beta \quad (2.1)$$

where  $\alpha > 0$  is related to the enthalpy and  $\beta$  is related to entropy. Both are experimentally determined constants depending on the composition  $f_A$ .

The covalent bond in the DBCP restricts the separation of the polymer chains and, in effect, prohibits macroscopic separation. For this reason, DBCPs are equipped with rich



**Figure 2.1** Schematic of a diblock copolymer. From [2].

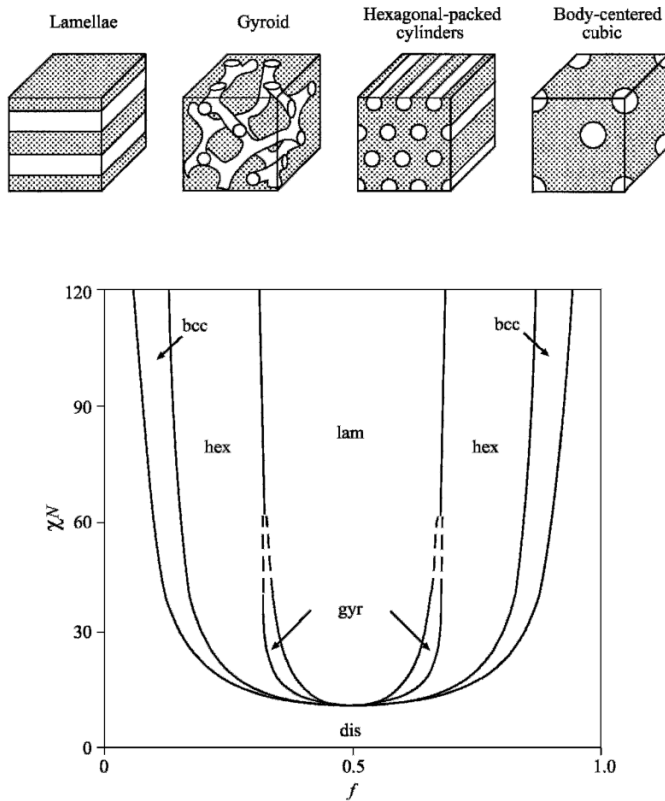


**Figure 2.2** Theoretical phase diagram of DBCPs based on self-consistent mean field theory. From [16].

phase behaviour depending on on  $\chi$ ,  $N$  and  $f_A$ . As one might expect, shorter chains and increasing temperature (decreasing  $\chi$ ) leads to a disordered system, while an increase in  $\chi$  and  $N$  allows the DBCP to locally separate on the scale of nanometers – also known in literature as *microphase separation*.

For this reason, the product  $\chi N$  dictates the phase behaviour of the DBCP and describes the strength of the segregation. For  $\chi N \ll 1$  the DBCP is in a disordered state. As  $\chi N$  approaches values on the order of 10, a transition to an ordered state occurs[2]. This is commonly known as the Order-Disorder Transition (ODT).

Depending on the composition  $f_A$  and  $\chi N$ , different structures are possible. Figure 2.2 shows a theoretical phase diagram based on self-consistent mean field theory[26] and a sketch of the possible structures. Note that, in most cases, navigating the phase diagram during an experiment is only possible along the vertical  $\chi N$  axis. Changing  $f$  requires the synthesis of a new polymer.

When obtaining the PS-*b*-PB diblock copolymer, values of  $f_A$  and  $N$  are usually not given. However, if the molecular weights  $M$  and densities  $\rho$  of the PS and PB blocks are known,  $N$  can be found using[29]:

$$N = \frac{M_{\text{PB}}/\rho_{\text{PB}} + M_{\text{PS}}/\rho_{\text{PS}}}{M_{\text{S}}/\rho_{\text{PS}}} , \quad (2.2)$$

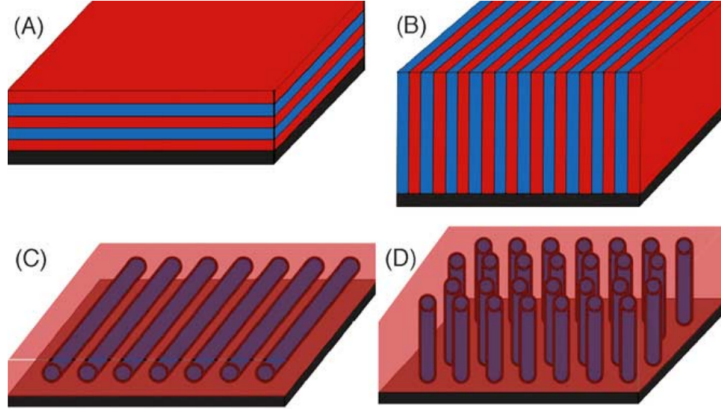


**Figure 2.3** Possible alignments in lamellar-forming (A,B) and cylinder-forming (C,D) DBCP thin films. From [35].

where  $M_S$  is the weight of the Polystyrene monomer. The polymer volume fraction of the Polystyrene block can be found using:

$$f_{PS} = \frac{M_{PS}\rho_{PB}}{\rho_{PS}M_{PB}}. \quad (2.3)$$

### 2.1.1 Diblock copolymer thin films

When confining a DBCP to a thin (5-50nm) film on a substrate, the system morphologies become much more complicated to describe theoretically. For lamellar-forming DBCPs, it has been suggested that film thickness and interactions at the interfaces (air and substrate) are important parameters[33].

Confining a DBCP to a thin film generally introduces an alignment of the structure either parallel or perpendicular to the substrate as illustrated in Figure 2.3. As mentioned in the introduction, the thermodynamic processes that governs the formation of the microdomains and alignment in thin films are still under investigation.

### 2.1.2 Diblock copolymer in solution

when introducing a solvent to a DBCP, the enthalpic interactions between the polymer chains are changed. This corresponds to a reduction in  $\chi$  to an effective Flory-Huggins parameter  $\chi_{eff}$ . Generally, this reduction can be approximated by[25]:

$$\chi_{eff} = \phi(\chi_{AB} + \Delta\chi) = \phi(\chi_{AB} + \chi_{A-S} - \chi_{B-S})$$

where  $\phi$  is the polymer volume fraction. For thin films, this is simply the ratio between the thickness of the dry and wet film

$$\phi = \frac{D_{dry}}{D}.$$

$\chi_{AB}$  is the interaction between the A and B block of the polymer as described by equation (2.1).  $\chi_{A-S}$  and  $\chi_{B-S}$  describe the solvent interaction with the A and B block, respectively. When the A and B blocks interact equally with the solvent, we say that the solvent is *nonselective* and obtain  $\chi_{eff} = \phi\chi$ [17].

In order to determine the selectivity of the copolymer blocks with regards to the solvent, the *Hildebrand solubility parameter*  $\delta_H$  is typically used. Qualitatively, materials with similar values of  $\delta_H$  are likely to be miscible. As the difference in solubility parameters of two materials ( $\Delta\delta_H$ ) decrease, the more easily they mix.

### 2.1.3 Solvent vapor annealing

The purpose of this thesis is to investigate the effects of solvent vapor annealing (SVA). By introducing/removing solvent from a sample, we can control  $\chi_{\text{eff}}$  and navigate the phase diagram from Figure 2.2 vertically. By varying the swelling/drying process, we aim to better understand the mechanisms of self-assembly.

As the microstructures are nanometer-sized objects, they are elusive to investigate directly. For this reason, x-ray scattering experiments are performed on the thin films in order to resolve the buried structures. The next section deals with the theory needed to understand the specifics of these experiments.

## 2.2 Scattering theory

In order to investigate the structures in the DBCP thin films presented in this thesis, it is advantageous to make use of x-ray scattering techniques. There are several reasons for this[34], but the primary advantage is the ability to monitor the experiment *in-situ*. Specifically, it is possible to get a spectrum roughly every 10 seconds while the experiment is running, providing valuable information about the structural changes over time.

The technique used in our experiments is known as *Grazing Incidence Small-Angle X-ray Scattering* (GISAXS). As the theory is a little involved, this section starts off with some general concepts from scattering theory in order to set the stage. This includes an introduction to *X-ray Reflectometry* (XR), which is a supplementary scattering technique that we make use of.

### 2.2.1 General concepts

This section provides some general concepts about scattering theory. It is primarily based on the introductory chapters in “Elements of Modern X-ray physics” by Jens Als-Nielsen and Des McMorrow[1].

Very briefly, X-ray scattering is a series of experimental methods widely used in many branches of materials science. As the structures of interest are smaller than the wavelength of visible light ( $\lambda < 100 \text{ nm}$ ), conventional microscopes lose their usefulness. To overcome this, samples are illuminated by X-rays ( $\lambda \approx 0.1 \text{ nm}$ ) and the scattered light can be measured to obtain information about the structure.

The typical scattering experiment is performed by illuminating a sample with an X-rays beam and measuring the scattered intensity  $I_{\text{sc}}$ . From classical electrodynamics, we know that the electric field of an electromagnetic wave is given by[13]

$$\mathbf{E}(\mathbf{r}, t) = \hat{\epsilon} E_0 \exp(i(\mathbf{k} \cdot \mathbf{r} - \omega t)),$$

where  $\hat{\epsilon}$  is the polarization vector,  $E_0$  is the amplitude of the wave,  $\mathbf{k}$  is the wavevector and  $\omega$  the frequency. The wavevector  $\mathbf{k}$  points in the direction of propagation and has the magnitude  $|\mathbf{k}| = 2\pi/\lambda$ . The intensity of an electromagnetic wave is proportional to the modulus square of the electric field:

$$I_{\text{sc}} \propto |\mathbf{E}|^2 = E_0^2. \quad (2.4)$$

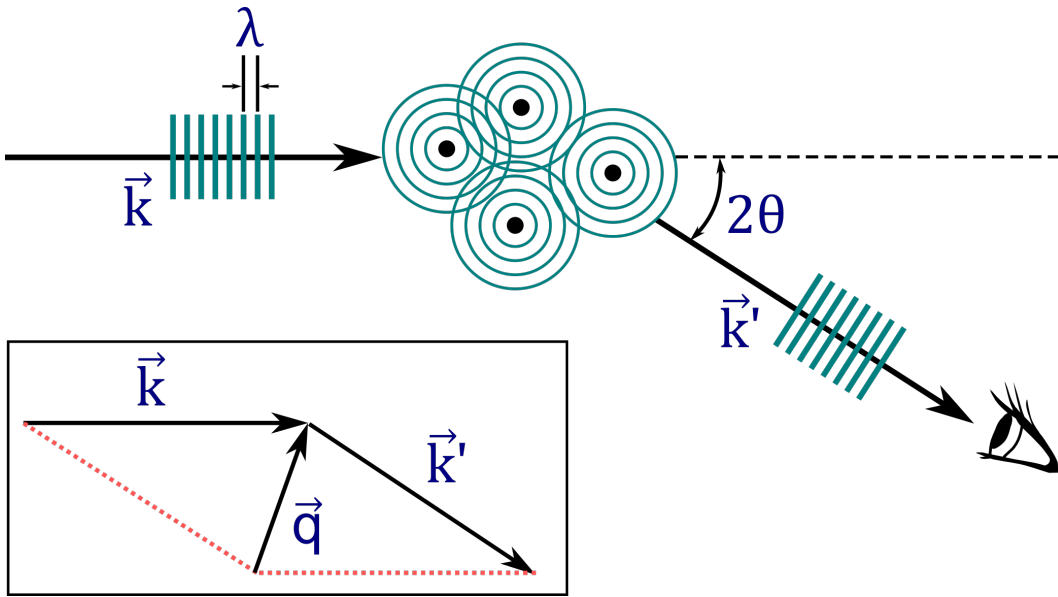


**Figure 2.4** The archetypical scattering experiment and scattering geometry. The scattering vector is defined as  $\mathbf{q} = \mathbf{k} - \mathbf{k}'$

Figure 2.4 illustrates the central concepts in a scattering experiment. An X-ray beam of wavelength  $\lambda$  impinges on the sample along the wavevector  $\mathbf{k}$  and the beam is scattered along  $\mathbf{k}'$  as the incident beam interacts with electrons in the sample. The detector is then able to record the intensity  $I_{sc}$  of the scattered x-rays at the angle  $\theta$ .

The primary physical process in classical X-ray scattering is the interaction between electromagnetic waves and matter. The electromagnetic wave exerts a force on electrons in the sample and the electrons, in turn, emit electromagnetic radiation as spherical waves. In the classical description, this process is *elastic* (momentum is conserved), and the wavelength of the scattered wave is equal to that of the incident wave. In the quantum-mechanical description, photons transfer energy to the electrons and there is a shift in the wavelength of the scattered photons. This process is known as *inelastic* scattering.

For the structures studied in this thesis, elastic scattering is the primary mechanism being exploited in order to characterize the system. For this reason, inelastic scattering is ignored for the remainder of this chapter.

In scattering theory, the geometry outlined in Figure 2.4 is generally adopted. The incident wave propagates along the wave vector  $\mathbf{k}$  and is scattered along  $\mathbf{k}'$ . The *scattering vector* is defined as  $\mathbf{q} = \mathbf{k} - \mathbf{k}'$ . Due to the elastic nature of the scattering, we have  $|\mathbf{k}| = |\mathbf{k}'|$ . As we shall see, the scattering vector  $\mathbf{q}$  turns out to be a natural way to describe a scattering process.

Because detectors record the scattered intensity, there is no information about the phase of the scattered beam (see equation (2.4)). For this reason, the scattered intensity is inherently ambiguous and it is generally impossible to reconstruct the sample using only the scattering data. To account for this, it is necessary to construct a model of the sample in order to interpret the scattering data.

How this model is constructed depends on the circumstances of the experiment, but there are some general features worth highlighting. In most cases, the model consists of a

*form factor* describing the constituents and a *structure factor* describing the arrangement of these constituents. As an example, the scattering from a single atom has the form factor

$$\begin{aligned} F(\mathbf{q}, \hbar\omega) &= \int_V \rho(\mathbf{r}) e^{i\mathbf{q}\cdot\mathbf{r}} d\mathbf{r} + f'(\hbar\omega) + i f''(\hbar\omega) \\ &= f^0(\mathbf{q}) + f'(\hbar\omega) + i f''(\hbar\omega) \end{aligned} \quad (2.5)$$

where  $\rho(\mathbf{r})$  is the electron density in real space and  $V$  is the volume of the atom. The functions  $f'$  and  $f''$  are dispersion corrections accounting for binding energies and absorption effects, respectively<sup>1</sup>. In the elastic approximation  $f'$  and  $f''$  are set to zero and the form factor is essentially a Fourier transform of the electron density. Furthermore, in the limit  $\mathbf{q} \rightarrow 0$ , the form factor is simply the atomic number  $F(\mathbf{q}) = Z$ . The usefulness of the Form Factor comes from the fact that the scattered intensity  $I_{sc}$  is the modulus square of the Form Factor:

$$I_{sc} = |F(\mathbf{q})|^2. \quad (2.6)$$

If a number of atoms compose a molecule, the total form factor of this arrangement is

$$F^{\text{mol}}(\mathbf{q}) = \sum_j F_j(\mathbf{q}) e^{i\mathbf{q}\cdot\mathbf{r}_j},$$

where the molecules each have form factor  $F_j(\mathbf{q})$  and position  $\mathbf{r}_j$ . To expand the model even further, these molecules can be placed on a crystal lattice where  $\mathbf{R}_n$  represents the position vector of lattice site  $n$ . The *total scattering amplitude* of the crystal then becomes

$$F^{\text{tot}}(\mathbf{q}) = [F^{\text{mol}}(\mathbf{q})] \cdot \sum_n e^{i\mathbf{q}\cdot\mathbf{R}_n}.$$

In this example, the form factor is  $F^{\text{mol}}(\mathbf{q})$  and the structure factor is  $\sum_n e^{i\mathbf{q}\cdot\mathbf{R}_n}$ . The thin-film system found in this thesis has a form factor consisting of cylinders with a homogeneous electron density and a structure factor being a two-dimensional hexagonal lattice. In Small-Angle X-ray Scattering (SAXS), particles are often diluted, so the form factor becomes a sum of all possible orientations  $\langle F(\mathbf{q}) \rangle$  and the structure factor goes to one (corresponding to no interaction between individual particles). Generally, X-ray scattering experiments measure contrast and regularity of electron density.

Having specified the model, we can express the scattered intensity  $I_{sc}(\mathbf{q})$  as a function of the scattering vector. Adopting the geometry from Figure 2.4, the length of  $\mathbf{q}$  can be expressed as a function of the scattering angle  $\theta$ :

$$|\mathbf{q}| = 2|\mathbf{k}| \sin \theta = \frac{4\pi}{\lambda} \sin \theta$$

Because  $\mathbf{q}$  is in units of inverse lengths, detector images are commonly referred to as being in *reciprocal space*. If the model is specified with the right assumptions and the experiment has good conditions, various properties of the sample can be derived from  $I(\mathbf{q})$ . A common, useful example is known as Bragg's Law, which gives the condition for constructive interference from a crystal lattice:

$$m\lambda = 2d \sin \theta \quad (2.7)$$

---

<sup>1</sup> Values of  $f'$  and  $f''$  are tabulated for atoms in the periodic table[18, 19]

where  $m$  is an integer and  $d$  is the distance between lattice planes. By measuring the distance between “bright” spots in reciprocal space, the distance  $d$  can be derived.

### 2.2.2 Reflection and refraction of x-rays

Due to the geometry of a GISAXS experiment, a treatment of x-ray reflection and refraction is needed. Like geometric optics in the visible range, reflection and refraction in a medium can be described through a refractive index  $n$ [38]. The refractive index depends on the frequency  $\omega$  of the incident light, and for X-rays it turns out that the refractive index is slightly less than unity. A consequence of  $n < 1$ , is that total external reflection is possible as x-rays pass from air to medium. The refractive index due to X-rays is expressed as

$$n = 1 - \delta + i\beta$$

where  $\delta$  is related to dispersion and  $\beta$  is related to absorption.  $\delta$  is on the order of  $10^{-5}$ , while  $\beta$  is on the order of  $10^{-8}$  and both can be derived from material properties. For our purposes the absorption contribution is ignored. By invoking Snell’s law[38], a good approximation of the critical angle can be found as

$$\alpha_c \approx \sqrt{2\delta}.$$

To describe the reflection and transmission at an interface, the Fresnel equations for X-rays can be worked out. To preserve consistency of the theory, these are represented in reciprocal space. The reflectivity  $r(q)$  and transmittivity  $t(q)$  at an interface is:

$$r(q) = \frac{q - q'}{q + q'} \quad ; \quad t(q) = \frac{2q}{q + q'} \quad (2.8)$$

where  $q$  is the wavevector magnitude of the reflected wave and  $q'$  is the wavevector magnitude of the transmitted wave. The corresponding intensity reflectivity and transmittivity can be found as the absolute square of  $r(q)$  and  $t(q)$ .

While this describes the behaviour at an interface, the details become somewhat more involved when applying the theory to a sample consisting of multiple layers of varying thickness and refractive index. This is due to the existence of multiple reflection/refraction events between layers. To account for these events, a method known as *Parratt’s exact recursive method*[31] can be applied.

Parratt’s method exactly solves the reflectivity of a system of  $N$  layers, each with thickness  $\Delta_j$  and refractive index  $n_j = 1 - \delta_j + i\beta_j$ . We want to describe the reflectivity amplitude as a function of the scattering vector  $r(q)$ . This is done through a recursive formula where  $r_{j,j+1}$  describes the reflectivity at interface  $j$  to  $j+1$ :

$$r_{N-2,N-1} = \frac{r'_{N-2,N-1} + r_{N-1,N} p_{N-1}^2}{1 + r'_{N-2,N-1} r_{N-1,N} p_{N-1}^2}, \quad (2.9)$$

where

$$p_j^2 = e^{i\Delta_j q_j}$$

and

$$q_j = \sqrt{q^2 - 8k^2\delta_j + i8k^2\beta_j}.$$

$r'_{j,j+1}$  is the the Fresnel reflectivity in the absence of multiple reflections (equation (2.8)). In order to solve the recursive equations, the substrate is assumed to be infinitely thick and not have any multiple reflections. In practice this means setting  $r_{N,N+1} = 0$  and then work out the equations recursively till the top layer is reached. After working through this procedure, we end up with the total reflectivity amplitude  $r_{0,1}$ , which is at the interface between the first layer and and vacuum.

The total reflectivity intensity  $|r_{0,1}|^2$  corresponds to a measurable quantity in an experiment. By varying the incident angle  $\alpha_i$  (effectively varying  $q$ ) over a suitable range and measuring the specular intensity, it is possible to obtain data to compare with equation (2.9).

It is important to note that the Parratt formalism only accounts for layers of homogeneous refractive index parallel to the surface. For this reason, X-ray reflectivity measurements only give information about the vertical structure of the film.

### Roughness

The Parratt formalism can be extended to include a roughness of the surface and interfaces. This can be done in a variety of ways, the simplest of which is an uncorrelated height profile  $h(x,y)$  describing the height  $h$  at a position  $(x,y)$  on the interface.

To account for this roughness in reflectivity studies, a *Nevot-Croce*[39] factor is added to the Fresnel reflectivities (without multiple scattering). The adjusted reflectivity  $\tilde{r}'_{j,j+1}$  is:

$$\tilde{r}'_{j,j+1} = r'_{j,j+1} \exp\left(-\frac{1}{2}(q_j q_{j+1})\sigma_j^2\right) \quad (2.10)$$

where  $\sigma = \sqrt{\langle h^2 \rangle}$  is called the root-mean-square roughness.

### 2.2.3 Grazing Incidence Small Angle X-ray Scattering

By combining the phenomena from sections 2.2.1 and 2.2.2, we can now describe a scattering experiment in reflection geometry. Specifically, this section describes Grazing Incidence Small-Angle X-ray Scattering (GISAXS). GISAXS is an experimental scattering method used in the characterization of interfaces and surfaces.

The geometry of a typical GISAXS experiment is outlined in Figure 2.5. The X-ray impinges on the sample at an incident angle  $\alpha_i$  and is scattered through an exit angle  $\alpha_f$  and an out-of-plane angle  $2\theta_f$ . Using this geometry and assuming elastic scattering, coordinates in reciprocal space become[28]:

$$\begin{aligned} q_x &= \frac{2\pi}{\lambda} [\cos(2\theta_f) \cos(\alpha_f) - \cos(\alpha_i)] , \\ q_y &= \frac{2\pi}{\lambda} [\sin(2\theta_f) \cos(\alpha_f)] , \\ q_z &= \frac{2\pi}{\lambda} [\sin(\alpha_i) + \sin(\alpha_f)] . \end{aligned}$$

The lateral scattering vector is defined as

$$q_{\parallel} = \sqrt{q_x^2 + q_y^2}$$

and is approximately equal to  $q_y$ . Samples in this thesis consist of a polymer film deposited on a substrate. Due to the difference in critical angle of the polymer and substrate, the experiment can be tuned to investigate different characteristics of the sample. Given that

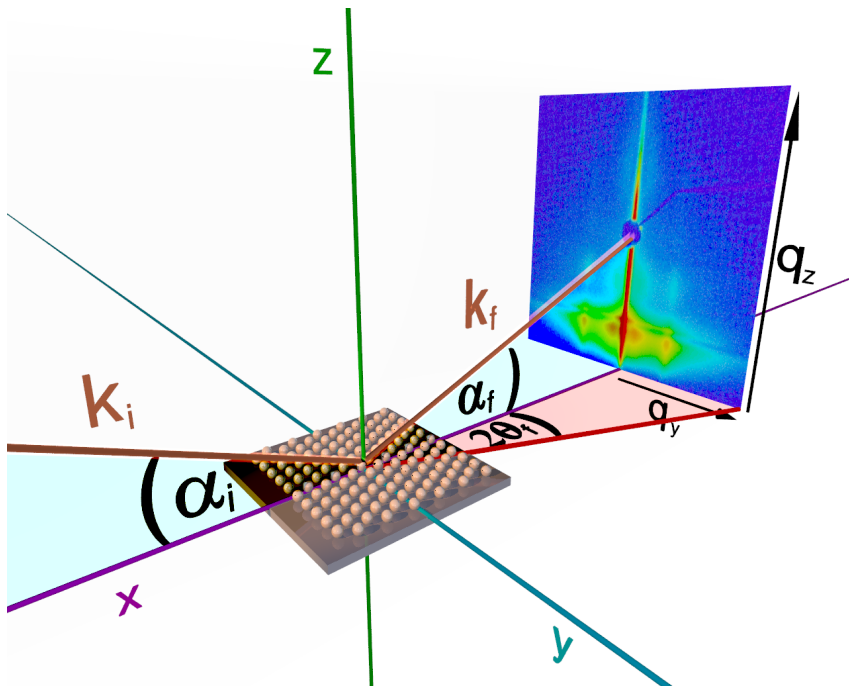


**Figure 2.5** GISAXS Geometry. Reprinted with permission from <http://gisaxs.de>[27].

$\alpha_{c,p}$  and  $\alpha_{c,s}$  are critical angles of the polymer and substrate and that  $\alpha_{c,p} < \alpha_{c,s}$ , three experimental regimes can be identified[28]:

- $\alpha_i < \alpha_{c,p}$ : Evanescent regime
- $\alpha_i > \alpha_{c,s}$ : Kinematic regime
- $\alpha_{c,p} < \alpha_i < \alpha_{c,s}$ : Dynamical regime

The evanescent regime takes its name from the *evanescent wave* that occurs along an interface during total external reflection. The evanescent wave typically has a penetration depth of a few nanometers[1], so this regime is only useful in the study of surface structures. The kinematic regime corresponds to an X-ray experiment in transmission geometry and probes the sample and substrate as a typical scattering experiment described in section 2.2.1.

In the dynamical regime, the X-ray is reflected off the substrate and, in effect, probes the inner structure of the film. As the inner structure of thin films is the focus of this thesis, all experiments are carried out in this regime. Other than restricting the beam path to the film, a significant advantage of this regime is the footprint effect[20] as illustrated in Figure 2.6. If a beam of height  $h$  impinges on a film of thickness  $d$  at an angle  $\alpha_i$ , the beam path has length  $\frac{2d}{\sin \alpha_i}$  and footprint  $\frac{h}{\sin \alpha_i}$ . Since  $\alpha_i$  is on the order of  $0.1^\circ$ , a GISAXS experiment is equipped with great statistical averaging due to illuminating a significant part of the sample.

Due to the geometry of a GISAXS experiment, the scattering theory has some added complexity compared to the treatment from section 2.2.1. In the dynamic regime, reflection events within the film contribute to the particle form factors. The Distorted-Wave Born Approximation (DWBA)[41] accounts for the first 4 terms of these events as illustrated

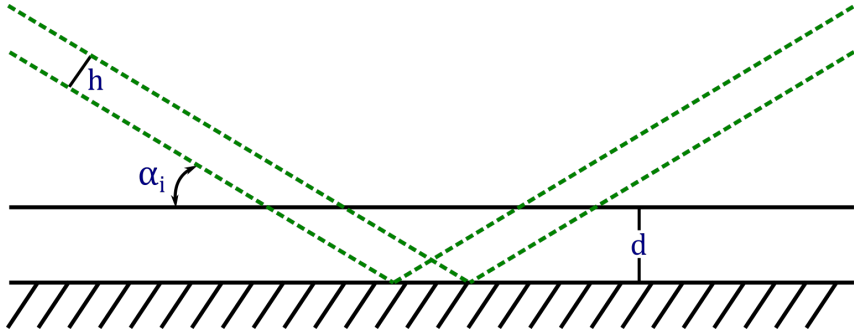


**Figure 2.6** The footprint effect. A beam of height  $h$  impinges on a film of thickness  $d$  at an angle  $\alpha_i$ . The beam path length in the film is  $2d/\sin \alpha_i$ . The footprint is  $h/\sin \alpha_i$ .

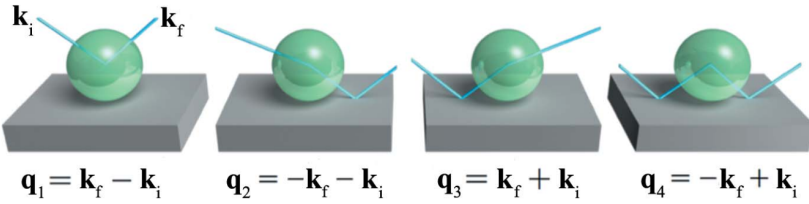


**Figure 2.7** The Distorted Wave Born Approximation. From [8]. The First term is the Born Approximation.

in Figure 2.7. A coherent sum of these events, weighted by the corresponding Fresnel reflectivities  $r_F$ , gives the effective form factor[34]

$$F_{\text{DWBA}} = F(\mathbf{q}_1) + r_F(\alpha_i)F(\mathbf{q}_2) + r_F(\alpha_f)F(\mathbf{q}_3) + r_F(\alpha_f)r_F(\alpha_i)F(\mathbf{q}_4). \quad (2.11)$$

In experiments with nano-structures, the form factors are typically expressed in terms of geometric objects (rather than atoms and molecules) and many of them are tabulated in literature[23]. As an example, a vertical cylinder of height  $H$  and radius  $R$  has the form factor:

$$F_{\text{cyl}}(\mathbf{q}, R, H) = 2\pi R^2 H \frac{J_1(q_{\parallel} R)}{q_{\parallel}} \sin_c\left(\frac{q_z H}{2}\right) \exp\left(-\frac{i q_z H}{2}\right), \quad (2.12)$$

where  $\sin_c$  is the cardinal sine and  $J_1$  is the Bessel function of the first order.

Similar to the form factor, the structure factor of a thin-film system has some additional theoretical considerations. Because the film thickness is comparable to the size of the embedded nano-objects, the structure factor  $S(\mathbf{q}_{\parallel})$  is generally described in two dimensions parallel to the film. Having defined the form factor and structure factor in the model, the scattered intensity can be found in the usual fashion:

$$I_{\text{sc}}(\mathbf{q}) = |F_{\text{DWBA}}|^2 S(\mathbf{q}_{\parallel})$$

As one might expect at this point, working out these models in practice can become rather cumbersome. For this reason, I have chosen to lean on the software program BornAgain[11]

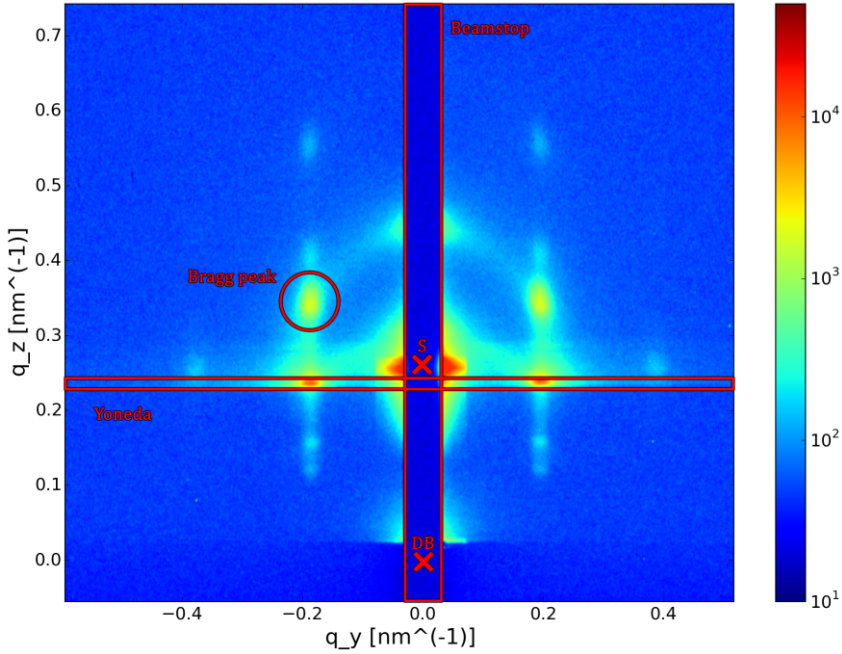


**Figure 2.8** Annotated GISAXS intensity map. DB is the direct beam and S is the specular peak. From the CHX-2013-01 experiment. 65 minutes into first drying,  $D = 469 \text{ nm}$  and  $\text{samx} = -0.4$ .

to implement the relevant models. In addition, theoretical treatment of vertical[43] and horizontal[24] cylinder structures exist in literature.

#### General features of GISAXS maps

In order to illustrate the features of a GISAXS spectrum, Figure 2.8 shows an annotated result from an experiment. The raw data consists of a  $1024 \times 1024$  matrix where each element represents the intensity at that point on the detector. To better distinguish details of the detector image, the values of this matrix are represented on a logarithmic color scale. The axes of the figure has been converted into reciprocal space in order to better analyze the data. This procedure requires some details about the experiment, and is explained in section 3.5.

The blue vertical bar is due to a *beamstop* – an object placed in front of the detector in order to block the high intensity of the direct (DB) and reflected (S) beam. The horizontal bar is known as the *Yoneda Band*[42] and is an area where the scattered signal is enhanced due to multiple scattering events within the film. This band is located between the critical angles of the polymer and substrate.

Lastly, Figure 2.8 feature a number of scattering peaks. These are interference patterns that allows us to analyze the film structure. While the details of this interference is complicated by the geometry, it is conceptually similar to Bragg's Law (equation (2.7)).

#### 2.2.4 Useful Conversions

When working with scattering models, material properties can be represented in a variety of ways. This section contains a short list of some useful conversions to be used later

on. In scattering theory, the scattering properties of a material is often described through the Scattering Length Density (SLD). The scattering length density is simply the electron density  $\rho_e$  [electrons/volume] multiplied by the Thomson scattering length  $r_0$ . The Thomson scattering length is a fundamental length in scattering experiments that describes the scattering ability of a single electron. It is expressed in fundamental units as

$$r_0 = \frac{e^2}{4\pi\epsilon_0 m_e c^2} \approx 2.818 \times 10^{-15} \text{ m}.$$

Knowing the composition of a sample, the electron density can be found as

$$\rho_e = \frac{\rho N_a}{M_a} f^0,$$

where  $\rho$  is the density,  $M_a$  is the molar mass,  $N_A$  is Avogadro's number and  $f^0$  is the atomic scattering factor from equation (2.5). As mentioned in section 2.2.1,  $f^0$  can be approximated by the atomic number  $Z$  when doing experiments with typical wavelengths ( $\lambda \approx 0.1 \text{ nm}$ ). In other cases, the values of  $f^0$  are tabulated in literature[18].

When working with GISAXS models, materials are often described through their refractive index  $n$  rather than by Scattering Length Density. Ignoring absorption effects, the refractive index is given by  $n = 1 - \delta$  and the value of  $\delta$  is given by:

$$\delta = \frac{\lambda^2 r_0}{2\pi} \rho_e.$$

Combining these expressions, the scattering length can be expressed in terms of  $\delta$ :

$$\text{SLD} \approx \frac{2\pi}{\lambda^2} \delta,$$

which is an approximation due to absorption being ignored.

## 2.3 Cylinder models

In this section, modelling of cylinder structures in relation to GISAXS experiments are investigated. This is done both through a review of existing literature and by simulations using the BornAgain software. As touched upon in section 2.1.1, thin films of cylinder-forming DBCPs tend to align either perpendicular or parallel to the substrate. With this in mind, models of standing and lying cylinders in thin films are investigated in the following sections.

### 2.3.1 BornAgain

BornAgain[11] is a software package developed for simulating and fitting GISAXS data. By constructing a sample using the BornAgain Python API, simulated GISAXS images are created and displayed. The Python scripts used to create the following simulations can be found in the Appendix.

### 2.3.2 Hexagonal packing of cylinders

In some cases[24, 43], cylinders in thin films have been observed to have a hexagonal packing. To assist the modelling, this section contains a few notes on the 2-dimensional hexagonal packing and how it relates to the sample parameters.

Given a hexagonal packing of standing cylinders and composition  $f_A$ , a relationship between the microdomain size (expressed through the radius  $R$  of the cylinders) and hexagonal spacing  $t$  can be found. Given a hexagon with a circle at each vertex and in the center, the circles inside the hexagon have total area

$$A_{\text{circles}} = 3\pi R^2,$$

where  $r$  is the radius of the circle. The hexagon itself has total area

$$A_{\text{hexagon}} = \frac{3\sqrt{3}}{2} t^2,$$

where  $t$  is the side length of the hexagon. The packing density (which is equal to the volume fraction) is then given by

$$f_A = \frac{A_{\text{circles}}}{A_{\text{hexagon}}} = \frac{2\pi R^2}{\sqrt{3}t^2} \quad (2.13)$$

and the limit case (hexagonal close packing) is when  $t = 2r$ , which gives packing density

$$f_A = \frac{\pi}{2\sqrt{3}} \approx 0.9069.$$

In many cases, experiments only provide information about the hexagonal spacing. By rearranging equation (2.13), the microdomain size (which is related to  $R$ ) can be expressed as:

$$R = \sqrt{\frac{2\pi}{f_A}} \frac{t}{3^{1/4}}. \quad (2.14)$$

Since  $f_A$  is known from the polymer, this can help estimate  $R$  in experiments and models.

### 2.3.3 Homogeneous film

In this section, I will briefly describe a model of a homogeneous film. The reason for this is to illustrate how the introduction of structure in the sample changes the GISAXS map. Figure 2.9 shows a simulated GISAXS map of a 200 nm homogeneous film with surface roughness  $\sigma = 5$  nm (see section 2.2.2). In the absence of surface roughness, only the direct and reflected beam will be visible as no scattering happens.

### 2.3.4 Standing Cylinders

In order to construct the standing cylinder model, we describe the sample through a set of parameters.  $D_{\text{film}}$  is the film thickness and  $R$  is the cylinder radius. In the case where the cylinders are arranged in a hexagonal lattice,  $t$  describes the center-to-center hexagonal spacing. Using equation (2.14), the cylinder radius is described through the polymer volume fraction  $f_A$  and hexagonal lattice constant  $t$ .

Lastly, The materials that make up the sample are described through their  $\delta$ -values (see section 2.2.2). As an initial probe, Figure 2.10 is a simulation of cylinders with no interference between them ( $S(\mathbf{q}) = 1$ ). The “rod-like” features of Figure 2.10 are a general feature of structure perpendicular to the surface commonly known as *Bragg rods*. The modulations in intensity is due to waveguide effects in the film[22].

To expand on the model, a structure factor can be added by modelling the interference between cylinders in the film. Due to the amorphous nature of the polymers, the interference

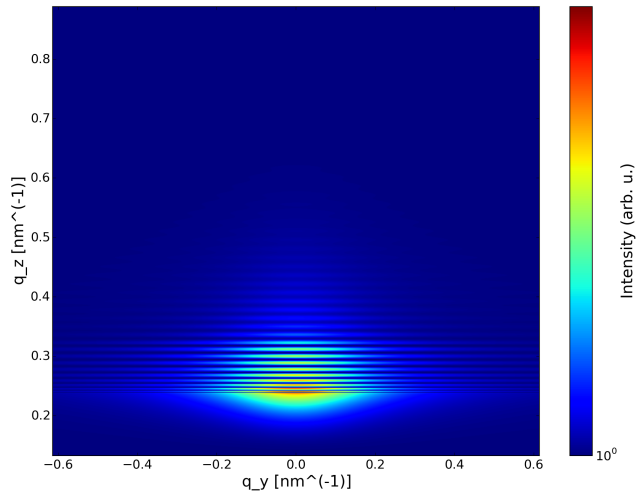


**Figure 2.9** Homogeneous flat film with  $D_{\text{film}} = 200 \text{ nm}$  and  $\sigma = 5 \text{ nm}$ .

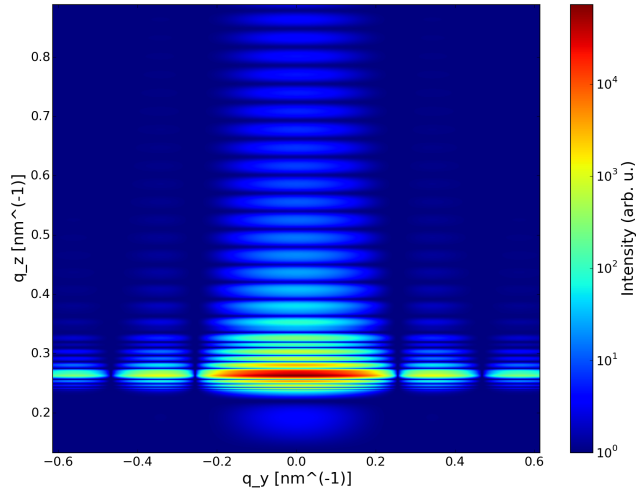


**Figure 2.10** Simulation of perpendicular cylinders in a thin film with no interference between cylinders.  $D_{\text{film}} = 200 \text{ nm}$ ,  $R = 15 \text{ nm}$ ,  $t = 34.1 \text{ nm}$  (calculated using  $f_A = 0.7$ ).

is typically described as a *paracrystal*[21]. A paracrystal is, as the name suggests, a state of matter that lies somewhere between a regular crystal lattice and a disordered system described through a pair-correlation function[28]. Briefly, the location of particles in a paracrystal are described through a probability density function and a set of lattice vectors.

In one dimension, the paracrystal is generated by placing a particle at the origin and then having a second particle placed with distance  $x$  described through a probability density  $p(x)$  that peaks at a mean value  $D$ . The third particle is then added a distance  $y$  from the second particle by a probability:

$$p_2(y) = \int_{-\infty}^{\infty} p(x)p(y-x)dx.$$

By iterating this, the pair correlation function can be built up step-by-step. In the examples presented here, a Gaussian probability density is used:

$$p(x) = \frac{1}{\omega\sqrt{2\pi}} \exp\left(-\frac{(x-D)^2}{\omega^2}\right). \quad (2.15)$$

The fourier transform of  $p(x)$  gives the probability density in reciprocal spacee

$$P(q) = \frac{1}{2} \exp\left(-\frac{q^2\omega^2}{4}\right) \exp(iqD)$$

and the structure factor is[24]:

$$S(q) = \text{Re}\left(\frac{1+P(q)}{1-P(q)}\right). \quad (2.16)$$

The fraction  $\omega/D$  is a measure of order in the system known as the *paracrystal distortion factor*. The paracrystal approach turns out to be a useful description in scattering experiments as it quantifies some common features of detector images; mainly the disappearance of higher-order Bragg peaks due to the lack of long range order. For  $\omega/D = 0.25$ , typically only first order Bragg peaks remain and  $\omega/D = 0.5$  resembles a disordered system[28].

When expanding the paracrystal model to two dimensions, four parameters are needed to describe the paracrystalline order; two distortions for each lattice vector<sup>2</sup>. In the case of hexagonal packing, all four order parameters are set to the same value due to symmetry.

Given these definitions, we end up with several parameters characterizing the final sample. An overview of these parameters are shown in Table 2.1. Figure 2.11 shows a simulation using the parameters from Table 2.1.

The geometric parameters in Table 2.1 were chosen to be representative for the system investigated herein.  $D_{\text{film}}$  is known from the WLI measurements and  $f_A$  is known from the polymer composition . The  $\delta$ -values were obtained from Di et al. [10]. The paracrystal distortion factor was chosen in order for higher order Bragg rods to remain (see Müller-Buschbaum [28] for details).

Qualitatively, Figure 2.11 only vaguely resembles the images we see in experiment. There are, however, some features that are worth highlighting. First, The distance  $d_y$  from  $q_y = 0$  to the first peak along  $q_y$  depends on the hexagonal center-to-center distance between the cylinders and can be approximated to the distance  $t$  in real space through:

$$t \approx \frac{2\pi}{d_y}. \quad (2.17)$$

<sup>2</sup> Similarly, a three-dimensional paracrystal needs 9 parameters.

**Table 2.1** Table of model parameters

	Description	Value
$D_{\text{film}}$	Film thickness	200 nm
$R$	Cylinder radius	15 nm
$f_A$	Polymer volume fraction	0.7
$\omega/D$	Paracrystal distortion factor	0.05
$\delta_{\text{PS}}$	PS $\delta$ value	$2.17 \cdot 10^{-6}$
$\delta_{\text{PB}}$	PB $\delta$ value	$1.88 \cdot 10^{-6}$
$\delta_{\text{Si}}$	Substrate $\delta$ value	$6.08 \cdot 10^{-6}$

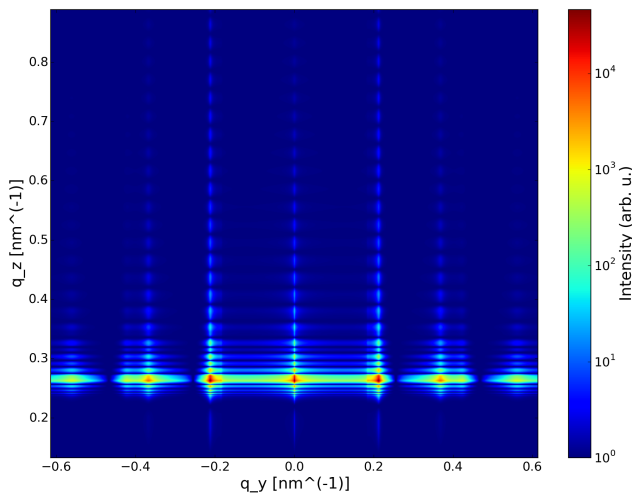


**Figure 2.11** Simulation of vertical cylinders in a thin film. Parameters used are shown in Table 2.1. The center-to-center hexagonal spacing is  $t = 34.1$  nm

Note, however, that the pattern observed in Figure 2.11 is very similar to (for example) a square lattice. As such, the precise geometry of the interference function can be difficult to infer from the detector image. Second, the paracrystal approach lets us quantify the lateral ordering of the cylinders through the appearance and disappearance of higher-order Bragg rods. This can be a useful feature when doing time-resolved GISAXS.

Finally, a complete analytical treatment of this system has been performed in great detail by Yoon et al. [43]. The results from this section correspond qualitatively well with their findings.

### 2.3.5 Lying cylinders

In modelling lying cylinders, some additional challenges come up due to the finite size of the vertical ordering. BornAgain only allows for interference functions in the  $(x, y)$  plane, so implementing lying cylinders in a hexagonal lattice is problematic.

In order to describe a hexagonal ordering of parallel cylinders, we turn to the work of Lee et al. [24]. This article present some theoretical results applicable to our system. Notably, Figure 2.12 is a simulation of horizontal cylinders in a hexagonal pattern along with a schematic of the geometry in real and reciprocal space.

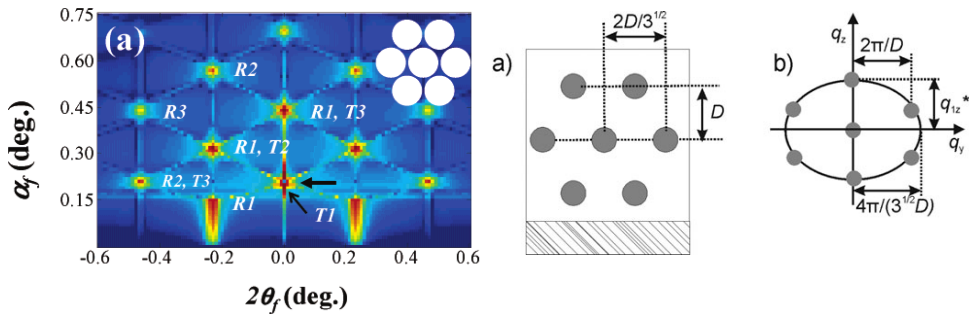


**Figure 2.12** **Left:** Simulation of lying cylinders in a hexagonal from Lee et al. [24]. R and T indicate diffraction peaks due to the transmitted and reflected beam, respectively. **Right:** Schematic of the dimensions in real and reciprocal space. From Papadakis et al. [30].

Figure 2.12 provides some useful tools in the characterization of lying cylinders. Fist, lying and standing cylinders can be qualitatively distinguished. In the case of lying cylinders, distinct peaks, known as *Diffuse Bragg Reflections* (DBR), appear in the detector plane. Furthermore, the hexagonal spacing can once again be found by measuring the distance to the first  $q_y$  peak similar to equation (2.17).

This concludes the, somewhat rudimentary, discussion of cylinder structures in thin films. As a short summary, the film structure can be characterized qualitatively by recognizing either Bragg Rods or Diffuse Bragg Reflections on the detector. The lattice spacing can be found by investigating the position of the  $q_y$  peak. Lastly, the degree of order (in terms of  $\omega/D$ ) in the system can be characterized by the sharpness of the peaks.

## 2.4 X-ray reflectivity

In this section, X-ray reflectivity (XR) experiment and data analysis is reviewed. While equation (2.9) describes the applied theory, there are some practical considerations worth mentioning.

The reflectivity experiment is performed by measuring the reflected beam as a function of incident angle (and in effect,  $q_z$ ). This data can then be compared with a model consisting of homogeneous layers according to the Parratt formalism contained in equation (2.9). As the modelling and fitting of XR data can be cumbersome, it can be advantageous to make use of an existing software package.

### 2.4.1 Choice of software

In [40] data analysis strategies for x-ray (and neutron) reflectivity data are reviewed. They find that genetic algorithms are “by far superior” to traditional methods, but that they may fail when layers are not well-defined.

GenX[5] is a software package for fitting X-ray and neutron reflectivity data using the differential evolution algorithm. This fitting strategy alongside the intuitive interface and flexible Python API has made GenX a obvious choice for working with reflectivity data. GenX utilizes the Parratt formalism for multilayers as described in section 2.2.2.

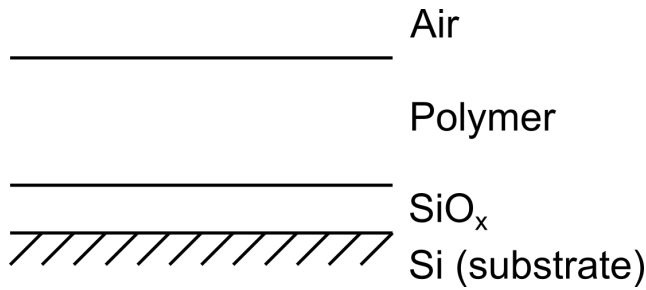


**Figure 2.13** Schematic of the XR model used in GenX.

## 2.4.2 Model

Following the analysis in [10], our sample is modelled as outlined in Figure 2.13. The substrate layer consisting of Si has roughness  $\sigma = 0$  and a fixed scattering length density (SLD). For the polymer and  $\text{SiO}_x$  layer, SLD, roughess and thickness can be left as fitting parameters.

## 2.4.3 Data preparation

To prepare for use in GenX, the reflectivity data are normalized through

$$R = \frac{\left( \frac{I_{\text{det}}}{I_{\text{mon}}} - \frac{I_{\text{back}}}{I_{\text{mon}}} \right)}{\frac{I_{\text{direct}}}{I_{\text{mon}}}},$$

where  $I_{\text{det}}$  is the intensity at the detector,  $I_{\text{back}}$  is the background intensity,  $I_{\text{direct}}$  is the direct beam and  $I_{\text{mon}}$  is the intensity of the incident beam.  $I_{\text{mon}}$  is needed in the normalization as the synchrotron beam decays over time. Furthermore, a normalization factor is used as a fitting parameter in GenX<sup>3</sup>. The beamline data is given as a function of the angle  $\alpha$ . I have chosen to convert this into  $q_z [\text{nm}^{-1}]$  through:

$$q_z = \frac{4\pi}{\lambda} \sin \alpha,$$

where  $\lambda$  is the wavelength of the incident beam. To automate this process, a Python method `reformat_data_for_genx()` has been implemented and provided in the appendix. Furthermore, a thorough technical description of reflectivity at the D1 beamline can be found at [37].

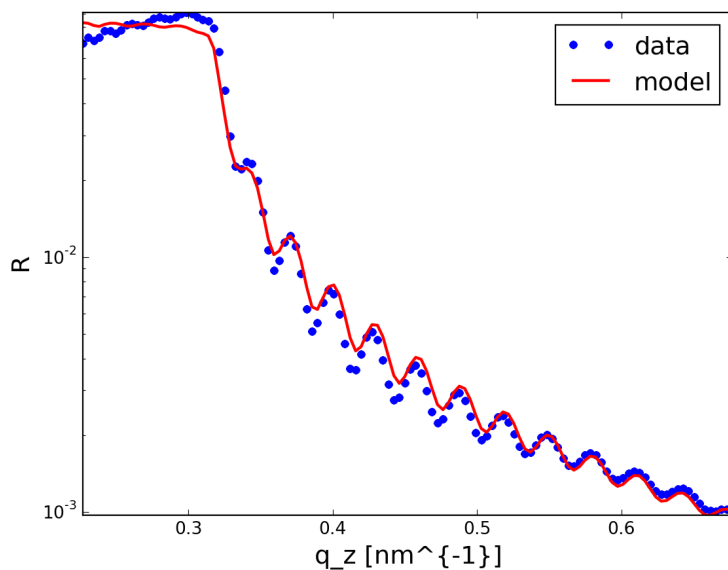
## 2.4.4 XR fitting strategies

Figure 2.14 is an example of an XR dataset and fit. The oscillations in the curve are known as *Kiessig fringes* and are due to interference of waves reflected from the top and bottom interfaces of the film[1]. The period of these fringes determine the film thickness. The damping of the curve in Figure 2.14 is due to the roughness of the film as described in section 2.2.2.

For this reason, it can be advantageous to leave out roughness as a fitting parameter if one is only interested in the film thickness. These features are also useful while doing experiments – a visual inspection of the XR data can hint at sample properties.

---

<sup>3</sup> This is known as `inst.setIO` in the program



**Figure 2.14** XR Example from the CHX-2012-02 sample. The fit obtains a film thickness of 194.7 nm. This value corresponds to the WLI measurement taken shortly before.



## 3 Experiment

The purpose of this chapter is to describe the details of the experiments performed at the D1 beamline, CHESS at Cornell University in Ithaca, New York. The experiments considered in this thesis range over three individual visits in 2012, 2013 and 2015. All three visits feature the same samples, solvents and a somewhat identical setup. Any differences will be noted throughout the chapter. Furthermore, the author was only present at the 2015 experiments, so details about the 2012 and 2013 are second-hand.

### 3.1 Materials

The diblock copolymer used in all experiments is cylinder-forming Polystyrene-b-Polybutadiene (PSPB) purchased from Polymer Source[32]. The chemical composition of PSPB is outlined in Figure 3.1.

Using equations (2.2) and (2.3) along with the molecular weights provided by Polymer Source allows us to determine the polymerization  $N$  and the polymer volume fraction  $f_{\text{PS}}$ . Using  $\rho_{\text{PB}} = 0.89 \text{ g/cm}^3$ ,  $\rho_{\text{PS}} = 1.05 \text{ g/cm}^3$ ,  $M_{\text{S}} = 104.149 \text{ g/mol}$ ,  $M_{\text{PB}} = 33700 \text{ g/mol}$ ,  $M_{\text{PS}} = 13600 \text{ g/mol}$ [32, 29], we obtain

$$N = 512$$
$$f_{\text{PS}} = 0.658.$$

The Flory-Huggins parameter follows the temperature dependence (see section 2.1)

$$\chi = \alpha T^{-1} + \beta,$$

where  $\alpha = 21.6 \pm 2.1$  and  $\beta = 0.019 \pm 0.005$ [29]. At room temperature ( $T = 300$ ), we get  $\chi_{\text{RT}} \approx 0.053$  and  $\chi_{\text{RT}} N \approx 27.14$ , which is well above the ODT. For the substrate, Silica (100) wafers were used. The solvents used for SVA are Cyclohexane (CHX), Toluene and Ethyl acetate (EAC). CHX is slightly selective for PB, Toluene is nonselective and EAC is slightly selective for PS. Table 3.1 shows the solubility parameters for the solvents and polymers.

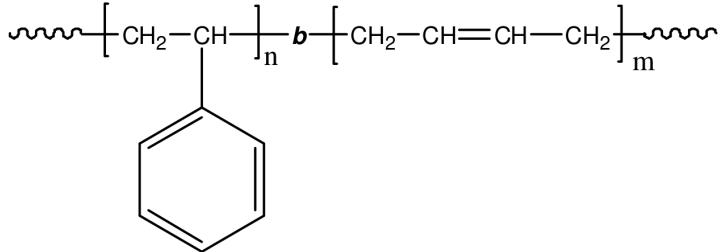


**Figure 3.1** Chemical composition of PSPB[32].

**Table 3.1** Hildebrand solubility parameters ( $\delta_H$ ) for substances relevant to the experiment[6].

Substance	Solubility parameter
Polybutadiene	$8.5 \text{ (cal cm}^{-3}\text{)}^{1/2}$
Polystyrene	$9.15 \text{ (cal cm}^{-3}\text{)}^{1/2}$
Ethyl Acetate	$9.1 \text{ (cal cm}^{-3}\text{)}^{1/2}$
Toluene	$8.9 \text{ (cal cm}^{-3}\text{)}^{1/2}$
Cyclohexane	$8.2 \text{ (cal cm}^{-3}\text{)}^{1/2}$

### 3.2 Sample preparation

The sample was prepared by dissolving the polymer in Toluene and adding Irganox to avoid crosslinking of the PB block[44]. In the 2015 experiments, Irganox was omitted from the procedure.

To prepare the thin film, a method known as *spin-coating* was used. By placing a drop of the polymer solution on a Silicon wafer and spinning at high speeds, the polymer is spread out evenly across the wafer due to a combination of the centripetal force, the viscosity and the surface tension. The spin-coating procedure also accelerates the evaporation of the solvent and eventually creates a dry, flat polymer film[15].

The properties of the final film depend on the spin speed, spin time and polymer concentration in the initial solution. In 2012 and 2013, the spin-coating procedure was performed at 3000RPM, while in 2015 it was performed at 6000RPM.

### 3.3 Solvent vapor annealing

Figure 3.2 shows a schematic of the SVA setup used in experiments. The *bubbler*s are bottles containing solvents relevant to the experiment. By submerging a tube containing nitrogen into the solvent, bubbles form, allowing small amounts of evaporated solvent to enter the chamber.

Note that in 2012 and 2013 only one bubbler was attached – the second bubbler was added to experiment with mixing of solvents. These experiments are outside the scope of this thesis, however.

The atmosphere in the chamber is controlled by the three flow controllers (marked 1,2 and 3) and valve A. Valve A is controlled by a simple on/off switch, while the flow controllers are controlled using computer software – either manually or through designated scripts.

A picture of the chamber is shown in Figure 3.3. Note that the vapor enters at high values of `samx`. The “diffuser” was added for the experiments in 2015, as previous experiments showed an inhomogeneity at high values of `samx`. The idea is to even out how the vapor enters the sample.

### 3.4 Thickness measurements

To follow the film-thickness during experiments, a White-Light Interferometer<sup>1</sup> (WLI) is placed above the sample chamber as shown in Figure 3.2. As mentioned in section 2.1.2, this data can be used to find the polymer volume fraction  $\phi$ . The WLI measurements are done with time intervals of roughly a second and are accurate to the order of nanometers.

<sup>1</sup> FilMetrics F30 spectroscopic reflectometer

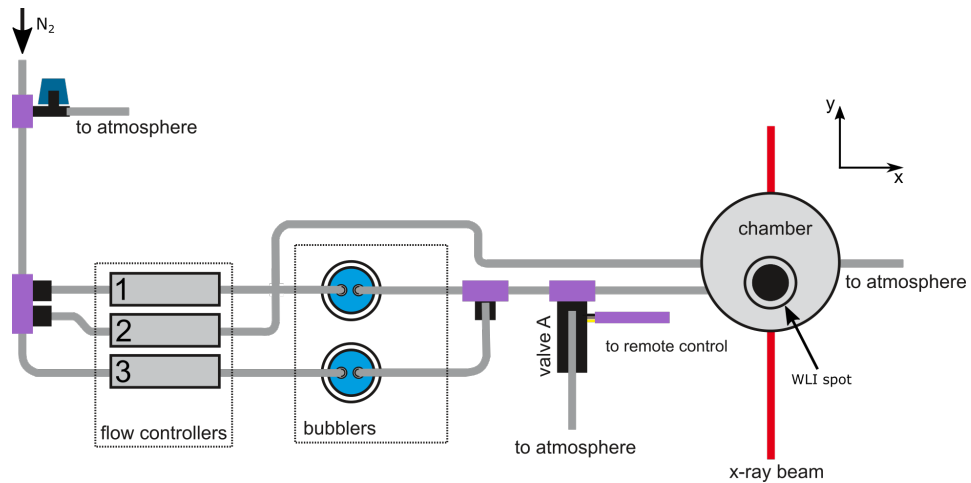


**Figure 3.2** Schematic of the SVA setup. Created by Anatoly V. Berezkin.

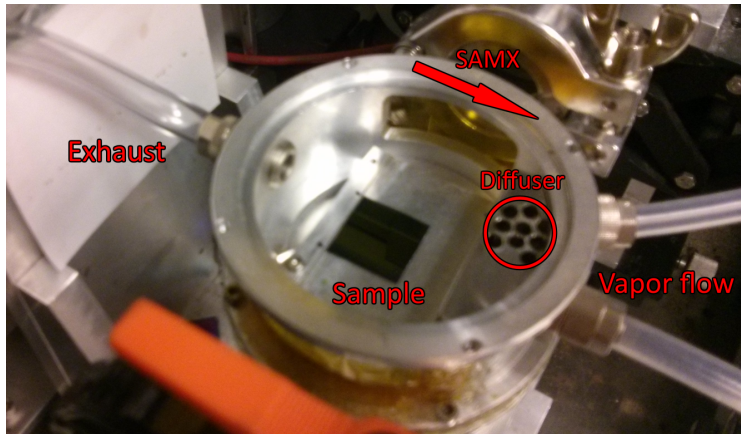


**Figure 3.3** Sample chamber.

### 3.5 GISAXS

GISAXS measurements were performed on the D1 beamline at CHESS. The X-ray beam has a wavelength  $\lambda = 0.116 \text{ nm}$ . The detector is a CCD camera with a pixel size of  $46.9 \mu\text{m} \times 46.9 \mu\text{m}$ . The sample-detector distance SD varied throughout the experiments, and is found by using AgBh as a reference as described below. The incidence angle is fixed at  $\alpha_i = 0.14^\circ$ .

GISAXS measurements are taken roughly every 10 seconds. To avoid damage to the film, the sample chamber is moved 0.3 mm along the  $x$ -axis (see Figure 3.2) between every measurement. The sample position on the  $x$ -axis is known as `samx`<sup>2</sup>.

#### *q*-calibration

Using Braggs law (section 2.2.1), the sample-detector distance SD, can be expressed in terms of the scattering vector  $q$ , a characteristic distance  $d$  and the wavelength  $\lambda$ :

<sup>2</sup> The `samx` name is adopted from the software controlling the experiment.

$$\text{SD} = \frac{q}{\tan(2 \arcsin(\frac{\lambda}{2d}))}.$$

Using this with a known substance allows us to calibrate the experiment. AgBh has a characteristic distance  $d = 5.838 \text{ nm}$ , so this can be used to find the sample-detector distance if the pixel size of the detector is known. Knowing the sample-detector distance, in turn, fixes distances in reciprocal space. For this reason, the necessary variables to perform data analysis are: pixel size, beam center, detector distance and wavelength. It is possible to fit all of these variables at once, but usually only the sample-detector distance is unknown.

### 3.5.1 X-ray reflectometry (XR)

To determine the thickness and roughness of the polymer film, X-ray reflectometry can be used alongside WLI measurements. The details of XR are described in section 2.4. In order to obtain the data for XR, the D1 beamline is equipped with a point-detector at the specular angle. By varying the incidence angle  $\alpha_i$  over the desired domain, a reflectivity curve is obtained. It is important to note that a sufficient reflectivity profile requires 300-500 points, so the film will likely be damaged after the procedure. For this reason, the XR measurements are done outside the  $x$ -axis range of GISAXS and never in the same spot.

# 4 Results

This chapter will present the results obtained from the D1 beamline at chess over the course of three separate visits. As mentioned in Chapter 2, there are some differences in the setup between the visits. I will try to emphasize these differences where applicable.

Due to the large number of experiments, they are categorized by solvent and year. Throughout the text, the naming scheme [SOLVENT] - [YEAR] - [ID] is used. As an example, CHX-2013-04 refers to the fourth experiment using Cyclohexane in 2013. Furthermore, the data from 2015 will be treated separately due to the absence of Irganox in the sample.

## 4.1 Procedure

This section is an outline of the procedure used in the data analysis. To give a better understanding of the steps taken, the procedure is exemplified via the CHX-2012-01 dataset. The reason for this choice is that the data shows some promising results, but also because it exemplifies some of the problems with the experiment. Generally, the steps taken during data analysis are the following:

1. View data
2. Synchronize data
3. Perform line integration
4. Perform peak fitting on integrated profiles
5. Perform fitting of reflectivity data
6. Summarize

### 4.1.1 View data

The data obtained in the experiments are: Thickness measurements, GISAXS images, X-ray reflectivity curves and a datafile with information about the GISAXS images. Doing a preliminary, manual inspection of these data immediately reveals some crucial details about the experiment.

The thickness measurements yield information about the polymer volume fraction  $\phi$  (see section 2.1.2). Specifically the minimal value  $\phi_{\min}$ , corresponding to the maximal swelling of the film, turns out to be an important parameter in quantifying the structural changes. In the case of CHX-2012-02, we obtain  $\phi_{\min} = 0.49$ .

The raw GISAXS images can be used to infer the morphologies via a visual inspection. As seen in section 2.3, the GISAXS images will have qualitative features depending on the orientation and order of the cylinder morphologies. Figure 4.1 shows six images taken during the first swelling (A-C) and drying (D-F). Figure 4.1 displays a rich variety of features. We see what looks like standing cylinders in a disordered lattice (A), standing cylinders in an ordered lattice (B), lying cylinders in an ordered lattice (C,E) and lying cylinders in a disordered lattice (D,F). There is a clear switch from standing to lying cylinders.

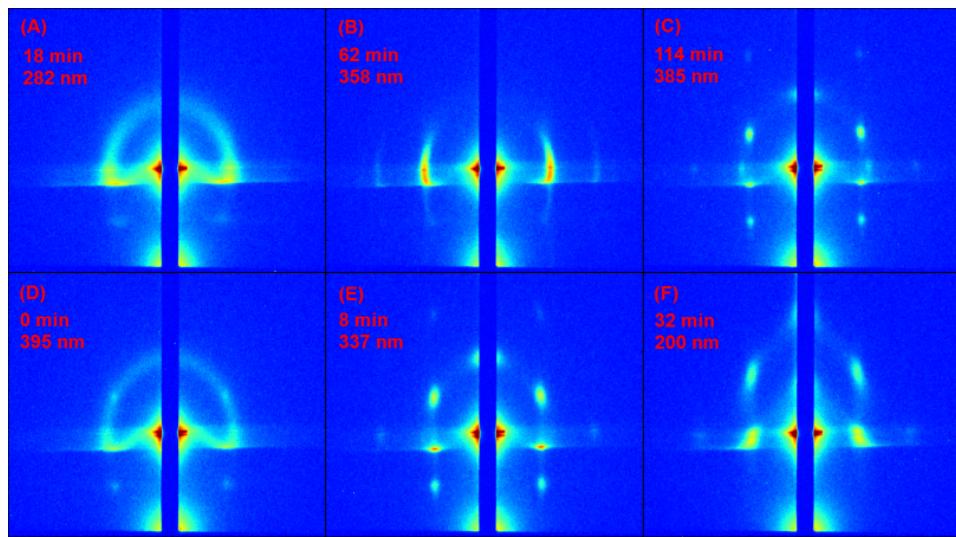


**Figure 4.1** Examples of GISAXS maps from CHX-2012-01. The displayed time is calculated from when the swelling (A-C) or drying (D-E) started. The `samx` values are as follows: (A) 6.1 (B) 7.1 (C) -0.4 (D) 1.1 (E) -0.4 (F) 2.6.

#### 4.1.2 Synchronize data

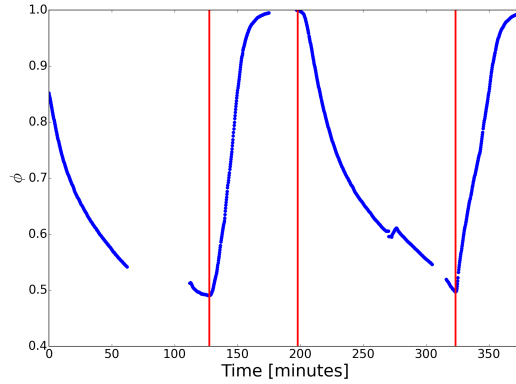
In order to perform any meaningful quantitative analysis, the raw data needs to be processed. The GISAXS and thickness measurements are done independently, so it is necessary to synchronize them. In order to achieve this, a python script has been created (found in the Appendix). Using the thickness and GISAXS datafiles as input, the script creates a set of data consisting of the following columns:

1. GISAXS image number
2. Thickness in nm
3. Time in seconds
4. `samx` value

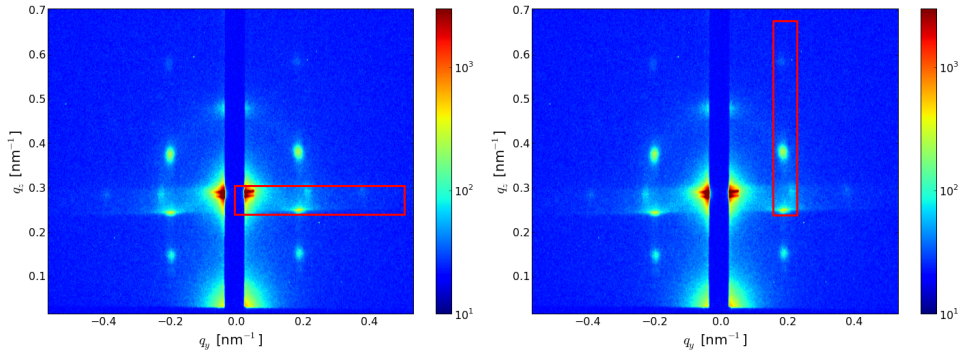
Having the data in this format, makes further processing of data much easier. The actual synchronization is done manually by supplying the script with a GISAXS and WLI datapoint occurring at the same time. For convenience, the script also contains a number of functions to plot GISAXS images and thickness data with relevant data attached. As an example, the time and thickness parameters in Figure 4.1 was found using the script.

Figure 4.2 shows thickness data of the CHX-2012-01 experiment generated by the script. As drying and swelling rates are thought to be important parameters in the experiment, it is important to clarify when the different phases of the experiment occurs. For the purposes of this analysis, phases in the SVA procedure is defined through minima/maxima of the film thickness. In Figure 4.2 this is indicated by vertical red lines.

The thickness plot in Figure 4.2 uses “real time” along the *x*-axis. When doing the experiments, collection of GISAXS and thickness data may be halted for a variety of reasons. Since dynamics play a central role in the experiments, these “gaps” are present in the plot. The big gap (roughly 60 minutes) in Figure 4.2 is due to losing the X-ray beam. The smaller gaps are scheduled breaks to do reflectivity measurements.



**Figure 4.2** Synchronized thickness data of CHX-2012-01. The red vertical lines mark the transition between the different phases (swelling, drying) in the experiment.



**Figure 4.3** Linecuts for CHX-2012-01. The boxes correspond to  $q_z = 0.27 \pm 0.03 \text{ nm}^{-1}$  (horizontal) and  $q_y = 0.19 \pm 0.03 \text{ nm}^{-1}$  (vertical).

#### 4.1.3 Line integration

In order to quantify the morphological changes observed from inspection of the GISAXS images, line integration can be performed using the software DPDAK[4]. By choosing a rectangular area on the detector image, the intensity is added up to a one-dimensional curve in either the horizontal ( $q_y$ ) or vertical ( $q_z$ ) direction. These areas are known as *line cuts* and is a valuable tool in quantifying features of the GISAXS image. Figure 4.3 show the chosen cuts for the CHX-2012-01 experiment.

The vertical cut is chosen in order to recognize the Diffuse Bragg Reflections indicating lying cylinders as seen in Figure 4.1(A). The horizontal cut is chosen in order to investigate three features. First, it can be used to recognize the second order peaks of horizontal structures as seen in Figure 4.1(B). Second, sudden changes in the position of the first order peak may indicate a change in cylinder orientation as seen in Figure 4.1(B) and (C). Third, the position of the peak provides us with the lattice spacing as described in 2.3.

As mentioned, The result of this integration is a 1-dimensional intensity profile for every GISAXS image processed. By converting each intensity profile to a logarithmic color map, the results of the line integration can be converted into a 2d-colorplot that follows the intensity profiles in time. Figure 4.4 shows the result of this procedure on CHX-2012-01.

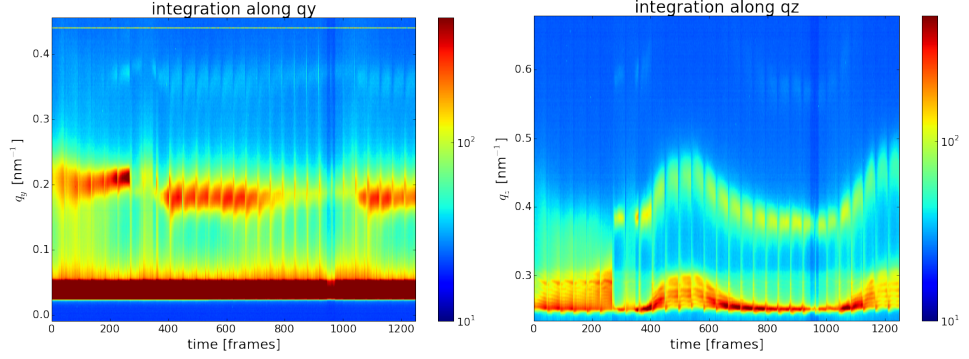


**Figure 4.4** 2d color plots of CHX-2012-01 along  $q_y$  and  $q_z$  using the integration areas from Figure 4.3.

Inspection of Figure 4.3 reveal information about the dynamics of the structural changes. Intensity peaks along both  $q_y$  and  $q_z$  appear as a result of the SVA procedure. Another feature of the colorplots is a periodicity in the measurements. This periodicity is an effect of moving the sample along `samx` and reveals an inhomogeneity in the film. To quantify both of these effects, peak fitting and filtering can be performed to further reduce the data.

#### 4.1.4 Peak fitting

To follow the position and sharpness of the peaks throughout the experiment, a peak fitting routine can be applied to the line integration data in order to extract information about diffraction spots. The peak fitting functions are determined by a combination of empirical inspection and trends from similar experiments. Inspired by Zhang et al. [44], the fitting along  $q_z$  is performed using a Gaussian function with a constant background:

$$f(q_z) = I_0 + A \cdot \exp\left(-\frac{4 \ln 2 (q_z - q_{z,p})^2}{w_z^2}\right).$$

For the integration along  $q_y$  a Lorenzian with constant background was used in the fitting procedure:

$$f(q_y) = I_0 + A \cdot \left[1 + 4 \left(\frac{q_y - q_{y,p}}{w_y}\right)^2\right]^{-1}.$$

In both cases  $A$  is the height,  $q_{z,p}$  ( $q_{y,p}$ ) is the peak position,  $I_0$  is the background, and  $w_z$  ( $w_y$ ) is the full width at half maximum (FWHM). In DPDAK, this is implemented using `GA( $q_{z,p}$ ,  $A$ ,  $w_z$ )` (`LO( $q_{y,p}$ ,  $A$ ,  $w_y$ )`) and `CB( $I_0$ )`. Figure 4.5 shows a peakfit of the vertical cut from Figure 4.3.

As illustrated by Figure 4.5, the peak fits cover a large fitting range. While this may introduce some uncertainty, it is necessary because the position of the peak moves during the experiment. Furthermore, the peaks appear and disappear as a result of the SVA procedure. To overcome this obstacle, the fitting parameters are filtered in the Python script that displays the result. Specifically, results that are outside a certain range of peak position and FWHM will be ignored. Furthermore, a filtering by `samx` value is possible.

The reason for these considerations are, simply put, to cut down the time required for data treatment. By filtering the results properly, thousands of GISAXS images can be

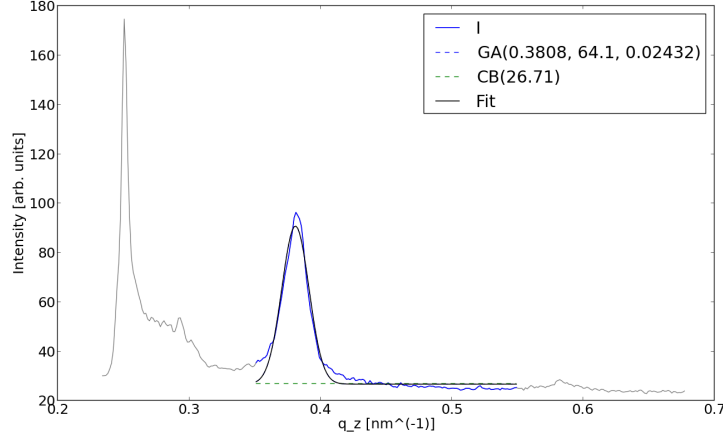


**Figure 4.5** Peakfit along  $q_z$  performed using DPDAK. The data corresponds to the vertical cut in Figure 4.3. The fit was done using a gaussian profile with constant background.

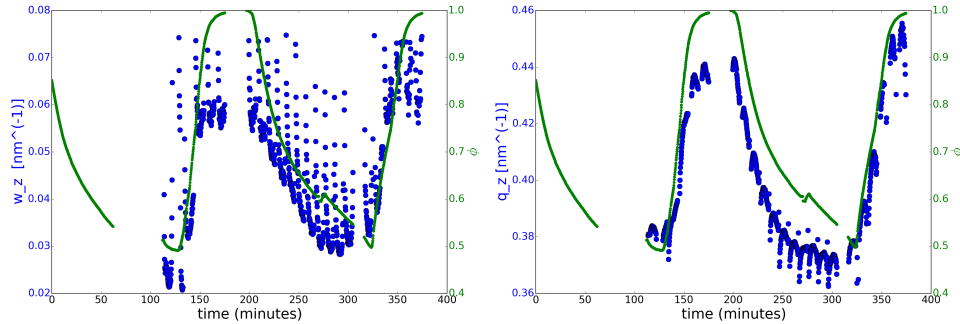


**Figure 4.6** Peakfit parameters of the  $q_z$  peak.  $w_z$  (left) and  $q_z$  position (right) alongside  $\phi$  for CHX-2012-01. Fits with  $w_z \in [0.01, 0.75]$  and  $q_z \in [0.36, 0.5]$  are included. The first peak appears at  $t = 113$  minutes when  $\phi = 0.51$ . Starting parameters for the fit are GA(0.41, 60, 0.02) and CB(25). Range is 0.34-0.41. Max iterations is 1000.

processed at once. However, as fitting procedures can be fickle, it is advantageous to review the results. DPDAK allows for a mass export of the fitting results in the form of images similar to Figure 4.5. These images can then be reviewed before further processing.

The data from DPDAK can then be exported and viewed using the `show_phi_peakfit()` function in `D1Gisaxs.py` (found in the Appendix). By supplying the function with DPDAK results, the thickness data and filtering options, a graph containing peak details alongside the polymer volume fraction  $\phi$  can be made. Figure 4.6 displays such a graph for the  $q_z$  peak in the CHX-2012-01 experiment.

Figure 4.6 displays some of the properties that were seen qualitatively in the color plot (Figure 4.4). The peak does not appear until after the “break” and the position moves in the positive  $q_z$  direction as the film is dried. Furthermore  $w_z$  increases as the film is dried, indicating a loss of order in the drying phase. Furthermore, the periodicity of the data is visible.

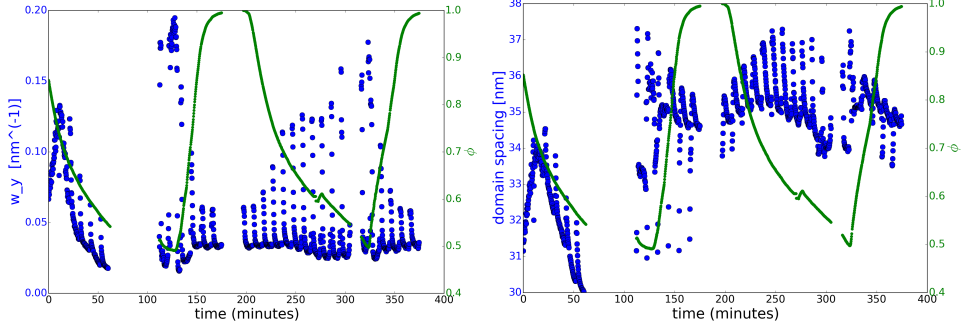


**Figure 4.7** Peakfit parameters of the first order  $q_y$  peak.  $w_y$  (left) and domain spacing (right) alongside  $\phi$  for CHX-2012-01. Fits with  $w_y \in [0.01, 0.04]$  and  $q_y \in [0.1, 0.3]$  are included. Starting parameters for the fit are L0(0.18, 100, 0.04) and CB(30). Range is 0.1-0.3. Max iterations is 1000.

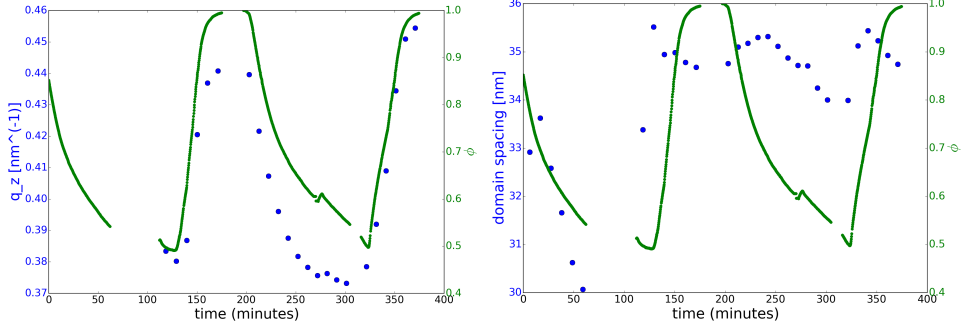


**Figure 4.8** Peak positions along  $q_z$  (left) and domain spacing (right) at  $\text{samx} = 4.1$ . Parameters from Figure 4.6 and 4.7 are used.

Figure 4.7 displays the same procedure performed along the horizontal ( $q_y$ ) linecut. As the position of the  $q_y$  peak is an indication of the lattice spacing, the values are converted into a domain spacing  $d_y$  through:

$$d_y = \frac{2\pi}{q_y}.$$

In Figure 4.7 we see the “sudden” shift in the domain spacing position when the orientation of the cylinders change. Furthermore, the standing cylinder order increases throughout the initial swelling.

To accommodate the problem of periodicity, it can be advantageous to filter out certain  $\text{samx}$  values. Figure 4.8 shows the  $q_z$  position and domain spacing at  $\text{samx} = 4.1$ . Qualitatively, the results are similar to the unfiltered figures, but the evolution is a little less noisy.

Finally, we note that a 2<sup>nd</sup> order peak along  $q_y$  happens during the swelling. This has proven difficult to characterize through peak fitting because of the weak signal. For this reason, the time and  $\phi$  of the first appearance is simply noted. The reason for this, is the fact that this peak seems to appear just before the switch to horizontal cylinders.

### 4.1.5 XR fitting

X-ray reflectivity data obtained throughout the experiment can be used to verify thickness obtained by the Filmetrics equipment. The method is explained along with an example in section 2.4. For the CHX-2012-01 sample, it has proven difficult to obtain data about the scattering length densities and roughness of the sample. However, by setting roughness to 0 and fitting the Kiessig fringes, the results of WLI and XR only deviate by a few nanometers.

### 4.1.6 Summarize

In order to compare the experiments, I have chosen to summarize the results through the following parameters.

1. value of  $\phi$  and  $t$  when at max swelling.
2. value of  $\phi$  and  $t$  when we see the first 2<sup>nd</sup> order  $q_y$  peak.
3. value of  $\phi$  and  $t$  when we see the first  $q_z$  peak.

In the case of CHX-2012-01, the parameters are  $\phi_{\min} = 0.49$  at  $t = 127$  minutes,  $\phi_{qy} = 0.58$  (first  $q_y$  peak) at  $t = 47$  minutes and  $\phi_{qz} = 0.51$  (first  $q_z$  peak) at  $t = 113$  minutes. Note, once again, that the exact time for the appearance of the first  $q_z$  peak is unknown due to the gap in data.

## 4.2 List of experiments

The following is simply a list of the experiments performed using the naming scheme from earlier, along with the minimal value of the polymer volume fraction  $\phi_{\min}$  and an indication of the existence of peaks along  $q_y$  (2<sup>nd</sup> order) and  $q_z$ . As a service to people with access to the logbooks, the logbook names are also listed.

### Cyclohexane

Name	$\phi_{\min}$	$q_y$ peak	$q_z$ peak	logbook name
CHX-2012-01	0.49	yes	yes	C3
CHX-2013-01	0.47	yes	yes	C2
CHX-2013-02	0.49	yes	no	C4
CHX-2013-03	0.60	yes	no	C8
CHX-2013-04	0.67	no	no	C9
CHX-2013-05	0.60	no	no	C10
CHX-2015-01	0.46	no	no	PSPB03
CHX-2015-02	0.49	no	no	PSPB04

### Ethyl acetate

Name	$\phi_{\min}$	$q_y$ peak	$q_z$ peak	logbook name
EAC-2012-01	0.64	yes	yes	C4
EAC-2013-01	0.71	no	no	C5
EAC-2013-02	0.66	yes	yes	C6
EAC-2015-01	0.67	yes	no	PSPB02

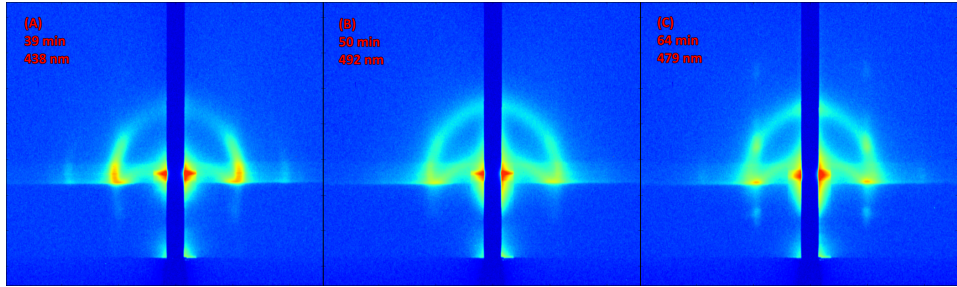


**Figure 4.9** Three consecutive GISAXS maps taken at the end of the first swelling phase in the CHX-2013-01 experiment.

### Toluene

Name	$\phi_{\min}$	$q_y$ peak	$q_z$ peak	logbook name
TOL-2012-01	0.70	no	no	C6
TOL-2013-01	0.68	no	no	C1
TOL-2013-02	0.63	yes	yes	C7

By applying the methods outlined for the CHX-2012-01 sample, the following sections will attempt to present the results organized by solvent. Experiments where no structural changes are observed will be, for the most part, ignored. Experiments performed in 2015 are treated separately.

### 4.3 Cyclohexane

In the case of Cyclohexane, structural rearrangements were only found in two experiments. CHX-2012-01 was treated throughout section 4.1 and we found rearrangements during the first swelling which was then “locked” throughout the experiment. The problem with CHX-2012-01 is the fact that the rearrangement happened when we lost the X-ray beam, so the details are speculation.

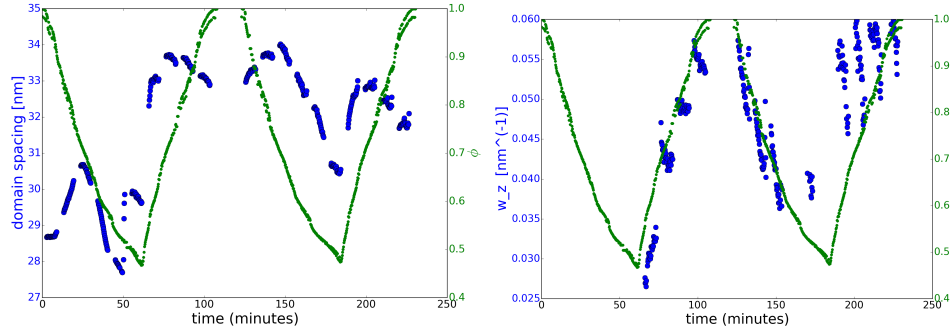
#### 4.3.1 CHX-2013-01

In CHX-2013-01, the experiment was repeated with very similar parameters to CHX-2012-01. We swell to the same  $\phi_{\min}$  value and qualitatively the same features are observed. It is important to note, however, that the initial film thickness is  $D_{\text{dry}} = 256 \text{ nm}$ , which is a 30% increase compared to CHX-2012-01. In effect, the fully swollen film has thickness  $D = 547 \text{ nm}$ .

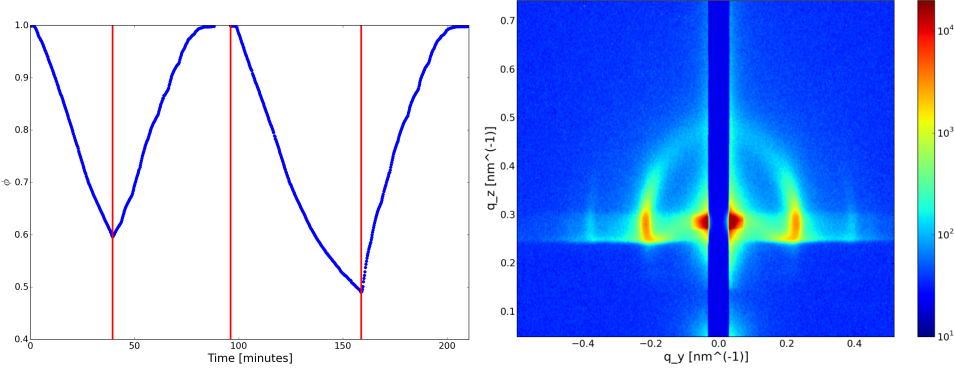
In CHX-2013-01, the transition to horizontal cylinders can be seen through a somewhat short, disordered phase. Figure 4.9 contains three GISAXS images taken towards the end of the first swelling. To quantify the dynamic features of this experiment, Figure 4.10 contain plots of  $w_y$  and  $q_z$  as a function of time for a selected range of  $\text{samx}$  values.

Figure 4.10 confirms the transition through a disordered phase seen in Figure 4.9. Using the conventions from Section 4.1.6, the CHX-2013-01 experiment is summarized as follows:

- Maximal swelling occurs at  $t = 61.4$  minutes, where  $\phi_{\min} = 0.47$
- First 2<sup>nd</sup> order  $q_y$  peak is seen at  $t = 38.5$  minutes, where  $\phi = 0.59$
- First  $q_z$  peak seen at  $t = 64.8$  minutes, where  $\phi = 0.53$



**Figure 4.10** **Left:** Domain spacing and  $\phi$  as a function of time from the CHX-2013-01 experiment. Fits with  $w_y \in [0, 0.2]$ ,  $q_y \in [0.15, 0.25]$  and **samx**  $\in [0, 8]$  are included. Line cut is taken at  $q_z = 0.26 \pm 0.025 \text{ nm}^{-1}$ . **Right:**  $q_z$  peak FWHM ( $w_z$ ) and  $\phi$  as a function of time. Fits with  $w_z \in [0.01, 0.06]$ ,  $q_z \in [0.3, 0.43]$  and **samx**  $\in [0, 10]$  are included. Line cut is taken at  $q_y = 0.19 \pm 0.015 \text{ nm}^{-1}$ .



**Figure 4.11** **Left:**  $\phi$  vs. time from the CHX-2013-02 experiment. **Right:** GISAXS image from the same experiment at  $t = 148.2$  minutes, where  $\phi = 0.54$ .

The remainder of experiments with Cyclohexane show no change in cylinder orientation.

### 4.3.2 CHX-2013-02

As one might have noticed from the table in Section 4.2, the CHX-2013-02 has a similar  $\phi_{\min}$  to the previous experiments, but no indication of horizontal cylinders. Furthermore the initial thickness is  $D_{\text{dry}} = 203.7 \text{ nm}$ , which is very similar to the CHX-2012-01 experiment. While this discrepancy is odd, the GISAXS maps have some weird features at certain **samx** values that may indicate skewed results. Furthermore CHX-2013-02 consists of two vapor treatment cycles that terminate at different  $\phi_{\min}$  values as shown in Figure 4.11.

With this in mind, a 2<sup>nd</sup> order Bragg rod was observed during the second vapor treatment as shown in Figure 4.11. The first vapor treatment terminated at  $\phi_{\min} = 0.60$  and feature no peaks. Maximal swelling ( $\phi_{\min} = 0.49$ ) was reached at  $t = 158.8$  minutes, roughly 10 minutes after the peak was observed.

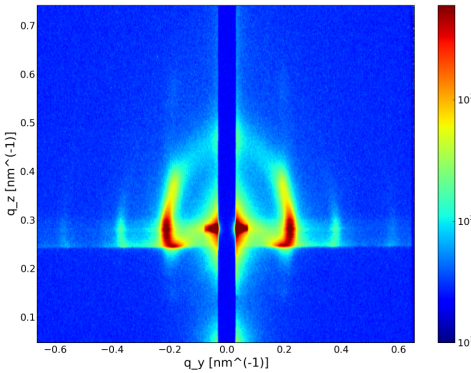


**Figure 4.12** GISAXS image from CHX-2013-03 at  $t = 50.7$  minutes and  $\phi = 0.77$ .

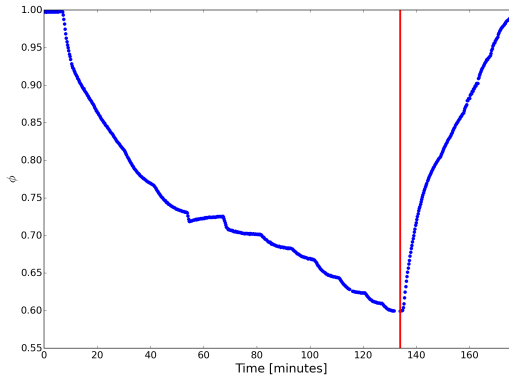


**Figure 4.13**  $\phi$  vs time for CHX-2013-05.

### 4.3.3 CHX-2013-03

The last experiment of interest is CHX-2013-03. While no change in morphology is observed, a very strong degree of order is reached for the vertical cylinders. Figure 4.12 shows a GISAXS image featuring 3<sup>rd</sup> order Bragg rods(!) taken at  $t = 50.7$  minutes, where  $\phi = 0.77$ . The first appearance of 2<sup>nd</sup> order Bragg rods was found at  $t = 32.5$  minutes with  $\phi = 0.61$ .

CHX-2013-04 and CHX-2013-05 are not discussed in depth due to their lack of distinctive features. It is noticeable, however, that CHX-2013-05 has no features interest when CHX-2013-03 does (both experiments has the same  $\phi_{\min} = 0.60$ ). For the sake of completeness, Figure 4.13 shows the  $\phi$ , time graph of CHX-2013-05.

## 4.4 Ethyl acetate

In the experiments with Ethyl acetate, the appearance of structural changes has been observed in two out of the four experiments. One common feature is the fact that the changes in orientation is `samx` dependant in all observed cases.

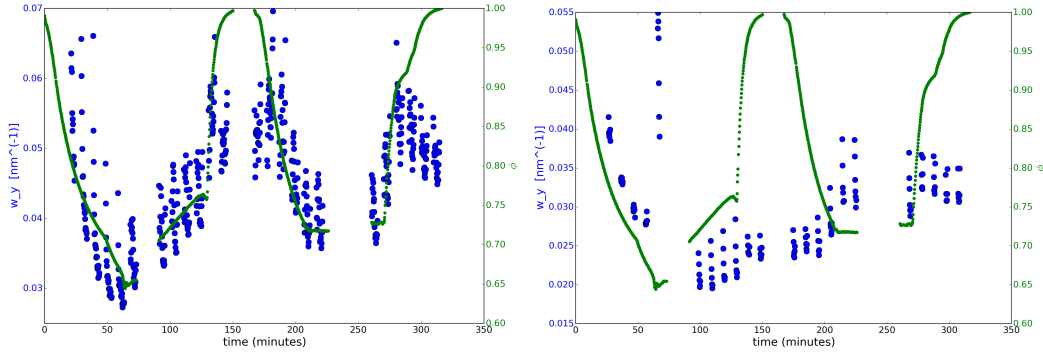


**Figure 4.14** Left: Peak FWHM ( $w_y$ ) and  $\phi$  as a function of time from the EAC-2012-01 experiment. Fits with  $w_y \in [0.01, 0.4]$ ,  $q_y \in [0.1, 0.3]$  and  $\text{samx} \in [-4, 3]$  are included. Line cut is taken at  $q_z = 0.27 \pm 0.025 \text{ nm}^{-1}$ . Right: The same data for  $\text{samx} \in [6, 8]$

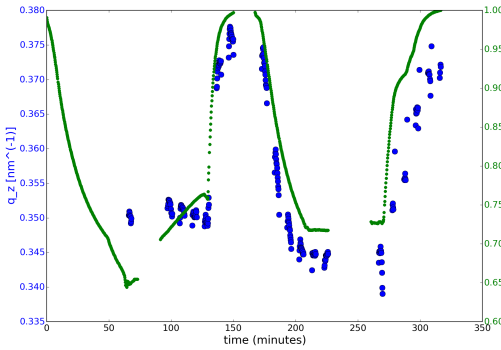


**Figure 4.15**  $q_z$  vs. time for the EAC-2012-01 experiment. Fits with  $w_z \in [0.01, 0.05]$ ,  $q_z \in [0.3, 0.45]$  are included. Line cut is taken at  $q_y = 0.17 \pm 0.015 \text{ nm}^{-1}$ .

#### 4.4.1 EAC-2012-01

To illustrate the `samx` dependence, Figure 4.14 shows a plot of  $w_y$  against time for two different ranges of `samx`. The data using  $\text{samx} \in [6, 8]$  shows a known pattern;  $w_y$  increases indicating a disordered state and then suddenly decreases to a horizontal cylinder morphology. Unfortunately, this change seems to happen when the GISAXS experiment was turned off.

Finally, Figure 4.15 shows the  $q_z$  peak position. We see that the peak appears just after the disordered state indicated by Figure 4.14. In conclusion, we note that the data is heavily dependant on `samx` and summarize:

- Maximal swelling at  $t = 64.3$ , where  $\phi_{\min} = 0.64$
- First  $q_z$  peak seen at  $t = 65.9$ , where  $\phi = 0.65$

Determining exactly when the 2<sup>nd</sup> order Bragg peak occurs has proven difficult due to the `samx`-dependance. A disordered state between the cylindrical orientations is not observed.

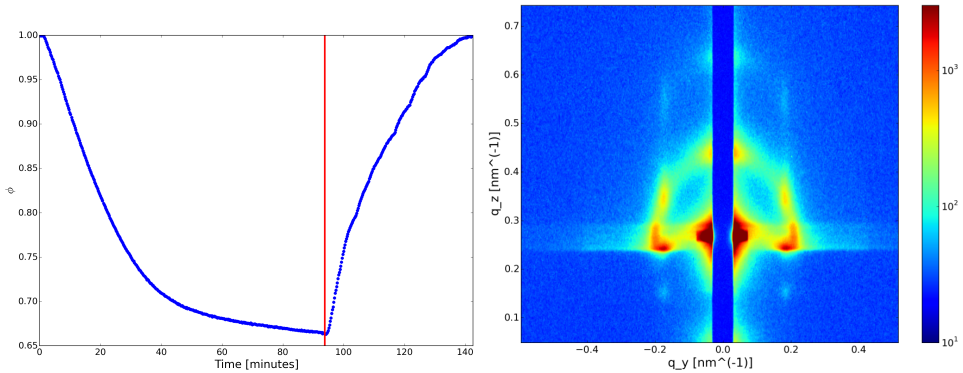


**Figure 4.16** **Left:**  $\phi$  vs time from the EAC-2013-02 experiment **Right:** GISAXS image from the same experiment taken at  $t = 82.5$  minutes,  $\phi = 0.66$ .  $\text{samx}$  is 7.9

#### 4.4.2 EAC-2013-02

As nothing interesting happens in EAC-2013-01, it is ignored apart from the data in section 4.2. In EAC-2013-02 there is, once again, a heavy  $\text{samx}$ -dependence. Furthermore, the obtained GISAXS images are qualitatively different from what has been shown in other experiments. For this reason, a representative GISAXS image will be shown, but no summary (in terms of timestamped events) is given.

Generally, the system looks disordered, with no sharp Bragg peaks in either direction. However, starting at  $t = 82.5$  minutes,  $\phi = 0.66$ , structure as shown in Figure 4.16 start to appear and persist around  $\text{samx} \in [7.9, 9]$ . Finally  $\phi_{\min} = 0.66$  occurs at  $t = 93.8$  minutes. A choice was made not to quantify this further. The structure in Figure 4.16 could indicate a combination of horizontal and vertical cylinders.

#### 4.5 Toluene

In the case of Toluene, only one experiment shows a switch to lying cylinders. TOL-2013-02 displays, once again,  $\text{samx}$ -dependant structural changes during SVA. As with EAC-2012-01, this dependence leaves time gaps in the data, making the details about the disordered transition state and 2<sup>nd</sup> order bragg peak difficult to resolve. Furthermore, the GISAXS images show features similar to EAC-2013-02. Figure 4.17 shows a  $q_z$  plot alongside a representative GISAXS map.

To summarize the available features, the  $q_z$  peak appears at roughly  $t = 70.8$  minutes when  $\phi = 0.68$ . Maximal swelling occurs at  $t = 122.8$  minutes when  $\phi_{\min} = 0.63$ . Note that this is the only evidence of rearrangements happening during swelling.

#### 4.6 2015

In the three experiments performed in 2015 the films were prepared without Irganox. This is suspected to “lock” the structure due to crosslinking as mentioned in section 3.2. This problem is mostly confirmed by the fact that we don’t see structural rearrangements despite reaching the same  $\phi_{\min}$  values.

With that in mind, there is still some information to extract from the experiments. The two experiments with Cyclohexane show basically no change in the GISAXS maps, so only

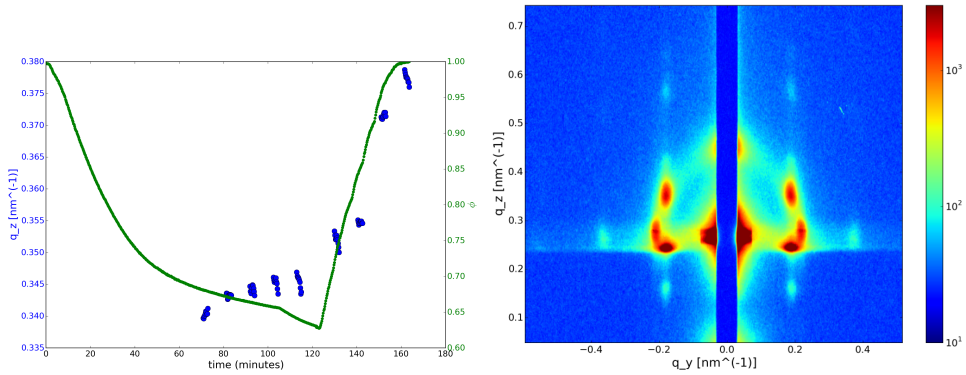


**Figure 4.17** Left:  $q_z$  peak vs. time for the TOL-2013-02 experiment. Fits with  $w_z \in [0, 0.06]$ ,  $q_z \in [0.3, 0.4]$ ,  $\text{samx} \in [7, 10]$ . are included. Line cut is taken at  $q_y = 0.20 \pm 0.015 \text{ nm}^{-1}$ . Right: GISAXS image from the same experiment taken at  $t = 131.1$  minutes,  $\phi = 0.74$  and  $\text{samx} = 8.5$ .

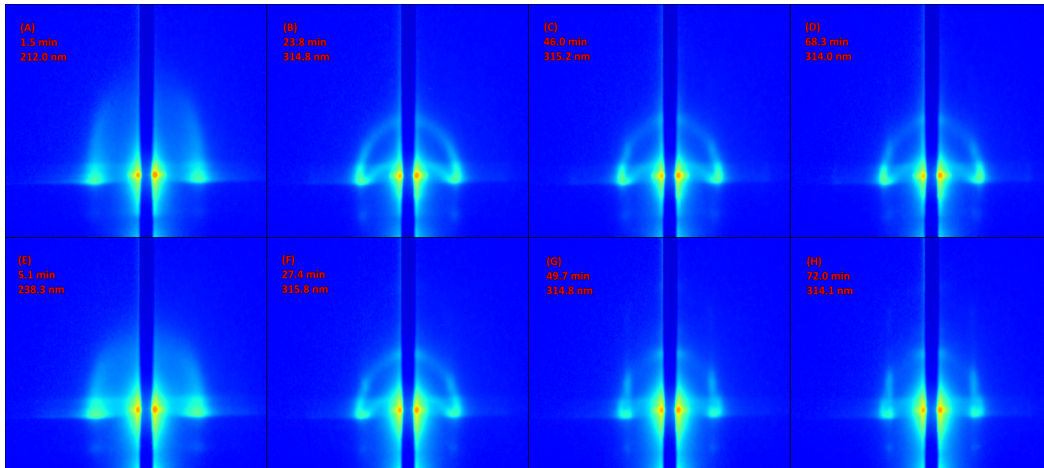


**Figure 4.18** GISAXS images during swelling from EAC-2015-01 at two different  $\text{samx}$  values. The top row (A-D) are at  $\text{samx} = -1.6$  and the bottom row (E-H) are at  $\text{samx} = 2.6$ .

EAC-2015-01 is considered here. In CHX-2015-01, we swelled the film to  $\phi = 0.67$  and kept it at this level for roughly an hour in order to investigate if a continuous vapor pressure over a longer time scale would affect the structure of the sample.

The qualitative result of this investigation is displayed in Figure 4.18. A few interesting features can be identified. First of all, the two series start out in similar configurations but evolve differently in time. Second, Figures 4.18(F) and 4.18(G) indicate a change in the structure over a fairly long timescale with no change in  $\phi$ .



## 5 Discussion

This chapter contains a discussion of a number of topics related to the experiments performed in this thesis. In addition to the experimental results, the methods used are given a critical look. Lastly, our observations are compared with relevant publications on similar diblock copolymer thin film systems.

### 5.1 General observations

The focus of this thesis is a determination of the parameters that control reorientation of cylinders from vertical to horizontal. While the data lacks details in certain areas, experiments that experience structural re-ordering generally go by the following scheme.

1. High degree of lateral order as indicated by 2<sup>nd</sup> order Bragg rod.
2. Switch to lying cylinders
3. High degree of ordering perpendicular to the film.
4. Loss of order and increase in domain spacing as the film dries

Furthermore, the CHX-2012-01 experiment goes through a disordered phase before switching to lying cylinders as shown in Figure 4.9. This disordered transition phase has not been observed for other experiments.

Interestingly, structural rearrangements have been observed with all three solvents and in every case there appears to be a threshold of  $\phi_{\min}$  that has to be crossed in order to change the cylinder orientation. However, this threshold does not seem to be the only parameter responsible for the structural changes.

In the case of SVA using Cyclohexane, CHX-2012-01 and CHX-2013-02 both reach  $\phi_{\min} = 0.49$  but only CHX-2012-01 sees the change to horizontal cylinders. The main difference between these two experiments is the swelling time, which suggests that timescales in the SVA procedure is important. CHX-2012-01 switches from well-ordered standing cylinders to lying cylinders in 20 minutes, whereas CHX-2013-02 only swelled for 10 minutes after the 2<sup>nd</sup> order  $q_y$  Bragg rod was observed. While inconclusive, these observations do signify that reordering happens on a timescale of several minutes.

The choice of using the 2<sup>nd</sup> order Bragg rod as a benchmark for timescales is somewhat empirical in nature. By just using the time for maximal swelling and first appearance of lying cylinders, the dynamics of the system before the switch is ignored. While no hard data about the timescales were available from the experiments contained in this thesis, using the 2<sup>nd</sup> order Bragg rod as an observational benchmark might be a useful tool in the future.

The  $\phi_{\min}$  thresholds observed for the different solvents are not surprising seen in the context of solvent selectivity (see section 2.1.2). Table 5.1 shows the  $\phi_{\min}$  threshold required for a switch along with the selectivity of the solvent. As the solvent becomes less selective for Polystyrene, a higher degree of swelling is required for the switch. Studies on lamellar PS-*b*-PB systems have suggested[44] that structural changes require a lowering of the Polystyrene

**Table 5.1** The effects of solvent selectivity on the threshold value  $\phi_{\min}$  required for a switch from standing to lying cylinders.  $\Delta\delta_{PS}$  is the absolute difference between the Hildebrand Solubility parameter of the solvent and Polystyrene.

Solvent	$\phi_{\min}$	$\Delta\delta_{PS}[(\text{cal cm}^{-3})^{1/2}]$
Ethyl Acetate	0.66	0.05
Toluene	0.63	0.25
Cyclohexane	0.49	0.95

glass transition temperature by introducing a solvent. The data in Table 5.1 supports this assessment as the more selective solvents can cause rearrangements at a higher value of  $\phi$ .

Lastly, the data from experiments performed in 2015 are unfortunately of little use. We did, however, observe position-dependant changes in the film. This is an interesting result as the experiments in 2015 were equipped with a “diffuser” as described in section 3.3. As will be discussed in the next section, this is supposed to create a position-independent atmosphere in the sample chamber in order to avoid the inhomogeneities from earlier experiments.

## 5.2 Inhomogeneity

A general trend in experiments across all experiment is the fact that we observe position-dependant structural changes in the film. This inhomogeneity imposed several challenges on the data analysis as seen in chapter 4. Before travelling to D1 in 2015, it was suggested that these inhomogeneities are related to the fact that the solvent vapor flow enters the chamber as described in section 3.3. This suggestion also agrees reasonably well with experiment; the structural changes generally happens at high values of `samx` which is close to the solvent vapor inlet.

However, in 2015 `samx`-dependant changes are still present as exemplified by Figure 4.18. How these changes are affected by the lack of Irganox is hard to say, but it does raise some interesting questions about the long-range effects of SVA. In particular, do the structural rearrangements happen locally? Is this a process that nucleates under certain circumstances?

Whatever the reason, the inhomogeneity in our experiment has a significant effect on the time resolution of the data. As indicated by Figure 4.18, a full scan across the sample takes roughly 20 minutes. This happens to be the timescale of rearrangements observed in the CHX-2012-01 experiment. For most of the inhomogeneous experiments, several ways of filtering the data by `samx` was attempted. The results were mostly inconclusive.

## 5.3 GISAXS modelling

In order to investigate the structure of the film, it is necessary to understand the GISAXS data to some extent. In this thesis, some amount of modelling was done on cylinder structures in thin films through the software package BornAgain (see Section 2.3).

While the result of this analysis was quite limited in usefulness, there are still a few strong points to take away from the efforts. As the theory of GISAXS in the Distorted-Wave Born Approximation is quite involved, having computer software help ease the modelling process can be useful. In the case of standing cylinders, implementing a relevant system was fairly

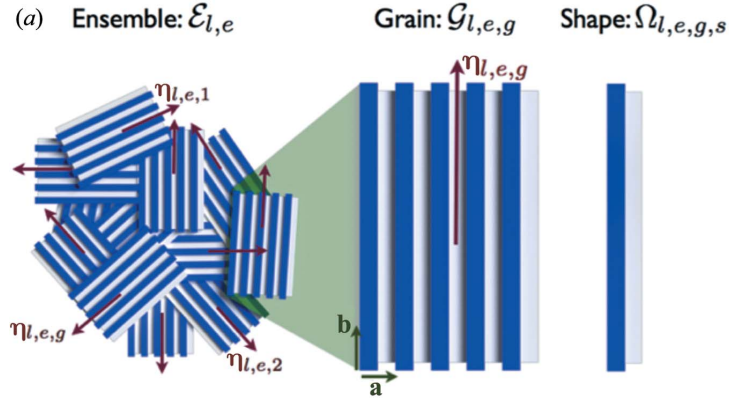


**Figure 5.1** HipGISAXS concept. From Chourou et al. [8].

straightforward and it can be quite helpful to see how the different parameters affect the output.

As beam-time is precious, another useful part of using computer software is as preparation. Within the software, it is fairly easy to change both geometrical (cylinder radius, film thickness) and experimental parameters (wavelength, incidence angle) and re-run the simulation. In the case of BornAgain, this can be done systematically through the Python API, as is demonstrated in the scripts provided in the Appendix.

For the purposes of this thesis, the simulations were primarily done as a tool to identify qualitative features in GISAXS maps. In short, Bragg rods were identified in the case of standing cylinders and spaced out Bragg peaks in the case of lying cylinders. When doing data analysis, the position and FWHM of those peaks were then found through peak fitting in order to extract structural parameters in the form of hexagonal spacing.

Optimally, one would strive towards fitting of GISAXS data to a model in order to extract even more structural parameters. While, to my knowledge, this has not been done to a significant extent, it is not unreasonable to expect this in the future. In the case of BornAgain, the software contains an extensive library of fitting routines along with a proof-of-concept script.

While BornAgain is a great tool due to its ease-of-use, there are still some disadvantages as demonstrated in the case of lying cylinders. As of this writing, interference functions can only be implemented in 2 dimensions. For this reason, it is worth mentioning the existence of the HipGISAXS[8] software package. In HipGISAXS, the model is constructed somewhat differently from BornAgain as demonstrated Figure 5.1.

The model is built from a shape (eg. a cylinder) that combine into grains in some periodic way (eg. a hexagonal lattice). These grains are then distributed in the ensemble in various ways. With this philosophy, concepts such as orientation distributions and grain sizes become a natural part of sample definition. In the work of Gu et al. [14], HipGISAXS is used to obtain details about a system of lying cylinders. For the purposes of this thesis, implementation of cylinder samples in HipGISAXS have not been attempted.

Finally, it is worth mentioning that both of the software packages mentioned are fairly new. In fact, while this thesis was prepared, both BornAgain and HipGISAXS received several updates. With this in mind, it is not unreasonable to expect more sophisticated modelling and fitting of GISAXS data in the future. However, one still has to keep in mind the ambiguous nature of scattering experiments. As models become more sophisticated,

the number of fitting parameters increase resulting in challenging fitting procedures. As discussed in the next section, this is a problem that is also encountered in X-ray reflectivity experiments.

#### 5.4 X-ray reflectivity

While X-ray reflectivity (see Section 2.4) was performed on several of the experiments treated in this thesis, not much attention was spent on the data analysis. The main reason for this is the lack of additional information and ambiguity of said information. That being said, XR appears to agree very well with the WLI measurements (see Section 3.4) when determining the film thickness. Throughout the data analysis, random samples of the XR data was done in order to compare with WLI. As the methods are similar in methodology they, unsurprisingly, yield similar results.

In the CHX-2013-02 experiment, the inhomogeneity was observed while the experiment was running and XR experiments were performed in both sides of the film after the 2<sup>nd</sup> vapor treatment and 2<sup>nd</sup> drying. Unfortunately, there is a high degree of roughness for the measurements taken at large  $\text{samx}$  values, effectively making the XR data treatment impossible. While unsuccessful, this demonstrates an advantage of XR when compared to WLI: The position of the measurement can be varied in order to detect inhomogeneities in the film.

With all these considerations, XR experiments have been somewhat unsuccessful in the present study. Several factors may have helped influence this. As seen in Section 2.2.2, the Parratt formalism used in XR modelling only accounts for structure perpendicular to the surface. The films discussed in this thesis feature significant in-plane structure which, in turn, may impact the XR experiments. Furthermore, the  $q_z$ -range and density of data-points has not been optimal in all experiments.

As a service to future experimenters investigating similar systems, I suggest doing XR over the range  $q_z \in [0.2, 0.6] \text{ nm}^{-1}$  with roughly 300-500 data-points in order to get sufficient statistics. With  $\lambda = 0.116 \text{ nm}$  this corresponds to  $\alpha_i \in [0.1^\circ, 0.3^\circ]$ .

#### 5.5 Data reduction

The bulk of the work in this thesis is concerned with data analysis of large amounts of data. In total, roughly 40 Gigabytes of data was processed. When working with the data, a couple of compromises had to be made in order to broadly represent the experiments.

As mentioned in Section 5.3, fitting of an entire GISAXS image is still somewhat out of reach. For this reason, peak fitting was performed in order to extract both qualitative and quantitative information about the structure. Qualitatively, the appearance of peaks in the  $q_z$  direction signifies a switch to lying cylinders. Quantitatively, the position and FWHM of peaks can be used to determine order and lattice parameters.

Peak-fitting in a “one-size-fits-all” fashion allows for quick analysis across a huge amount of data, but does come with a couple of caveats. As the peaks has a wide range of positions and shapes throughout the experiments, it was necessary to widen the search range and decrease the amount of fitting parameters in order to get reasonable results. Experimenting with, for example, an exponential  $q$ -dependant background resulted in some fits being better while others got worse. In short, the peak fitting functions from Section 4.1.4 were chosen in order to accommodate the largest amount of data in a reasonable way. The peak fitting was performed through the software package DPDAK and turned out to be a painless experience. It is fairly easy to set up, and peak fitting was reasonably fast.

In order to gain information about the film thickness and `samx` position, custom scripts had to be created. These allow for a synchronization of WLI thickness data and GISAXS image data so everything can be compared in a systematic manner. By including routines for visualization and import of DPDAK peak fits, the plots from Chapter 4 were easily created.

Due to the amount of data that can be generated at synchrotrons these days, the need for systematic data analysis increases. Hopefully, the present work demonstrates some of the advantages and disadvantages of one such data reduction.

## 5.6 Relevant results from literature

As mentioned in the introduction, the interest in thin film structure has recently (the last 5-10 years) attracted a lot of attention. The purpose of this section is to review publications on cylinder-forming DBCP thin films and compare with the results contained in this thesis. For a review of the SVA method, see Sinturel et al. [36]. For a general GISAXS review see Renaud et al. [34].

In the work of Gu et al. [14], Solvent vapor annealing of PS-*b*-P2VP was performed in order to characterize the ordering of lying cylinders after solvent removal. They find that domain spacing and lateral ordering if the final film can be controlled by  $\phi_{\min}$  and the rate at which solvent is removed. In particular, they find that the domain spacing  $D$  is related to the polymer volume fraction through

$$D \sim \phi^{2/3}.$$

While this power-law cannot be confirmed for the experiments carried out in this work, there are still some qualitative similarities. The ordering happens through a disordered state, FWHM and domain spacing increases during solvent removal.

Gowd et al. [12] investigates the pathways of cylinder orientations in PS-*b*-P4VP thin films by SVA with selective and non-selective solvents. In the case of a non-selective solvent, a standing cylinder morphology switches to a lying cylinder morphology through a disordered state. This is similar to our findings in the CHX-2013-01 experiment. In the case of a selective solvent, the standing cylinders go through an ellipsoidal phase during swelling and returns to standing cylinders during drying. These findings show that it is possible to navigate the  $(f, \chi N)$  phase diagram (see Figure 2.2) along the  $f$  axis through the use of selective solvents.

Similarly, Chavis et al. [7] show the possibility of navigating the phase diagram and retaining the structure in the dry film. By performing SVA with solvent mixtures on PHEMA-*b*-PMMA thin films, a wide range of morphologies were observed. By rapid drying, the morphology from the swollen state is kinetically trapped resulting in a dry film with the desired morphology.



## 6 Conclusion

In this thesis, the structural changes of cylinder-forming Polystyrene-*b*-Polybutadiene (PS-*b*-PB) diblock copolymer thin films was investigated using solvent vapor annealing. Due to the composition  $f_{\text{PS}}$  of PS-*b*-PB, the films are composed of PS cylinders in a PB matrix.

By exposing the film to solvent vapors the effective Flory-Huggins interaction parameter  $\chi_{\text{eff}}$  is decreased, allowing the blocks to undergo structural changes. Three solvents of varying selectivity were used: Ethyl Acetate (EAC), Toluene (TOL) and Cyclohexane (CHX).

In order to investigate these changes, time-resolved grazing-incidence small-angle x-ray scattering (GISAXS) was performed at the D1 beamline, CHESS at Cornell University in Ithaca, New York. X-ray Reflectivity (XR) was performed as a supplementary method, but did not yield additional information about the films.

Using a combination of qualitative and quantitative methods to determine the structure, re-orientations of the cylinders from a standing to a lying morphology was identified using all three solvents. Data analysis was performed through a combination of available software packages[11, 4] and custom Python scripts (found in the Appendix).

The re-orientation appears to depend on the minimal polymer volume fraction  $\phi_{\min}$  and solvent selectivity to the PS block. As such, different values were found for each solvent:  $\phi_{\min,\text{EAC}} = 0.66$ ,  $\phi_{\min,\text{TOL}} = 0.63$ ,  $\phi_{\min,\text{CHX}} = 0.49$ . The dependence of selectivity to the PS block can be explained by the fact that PS is in the glass phase at room temperature. Performing SVA lowers the glass transition temperature, allowing the PS cylinders to re-organize.

Due to inhomogeneities in the film, details about the dynamics of re-orientation was difficult to determine. However, in one experiment with CHX the switch from standing to lying morphology happens through a disordered phase over a span of 15 minutes. Further investigation of this timescale are left to future experiments.



# Appendix

## D1Gisaxs.py

`D1gisaxs.py` is a header file written in Python containing a number of functions used in GISAXS data analysis. Requires a Python installation with numby and matplotlib to work.

D1Gisaxs.py

```
1 from numpy import *
2 from pylab import *
3
4 # conversions (base is nanometer)
5 micrometer = 1e3
6 nanometer = 1
7 milimeter = 1e6
8 angstrom = 0.1
9 degree = 2*pi/360
10
11 # sync GISAXS and thickness data
12 # This function takes 4 variables
13 # t_data is a string with the relative path to the wli thickness data
14 # g_data is a string with the relative path to the gisaxs data
15 # t_index and g_index are the indices that syncronise the times of the two datasets
16 # It returns a dataset with gisaxs measurement number, thickness, time, samx (columns
17 # 0,1,2,3 respectively)
17 def gisaxs_thickness(t_data,g_data,t_index,g_index,d1_2013=False,d1_2015=False):
18     gisaxs_data = genfromtxt(g_data)
19
20     # data is formatted differently depending on when the experiment was performed
21     if (d1_2013 | d1_2015):
22         thickness_data = genfromtxt(t_data, delimiter=',',skip_header=9)
23         if d1_2015:
24             thickness_data = transpose(array([thickness_data[:,0],thickness_data[:,1],
25                                              thickness_data[:,2],thickness_data[:,6]]))
26         if d1_2013:
27             thickness_data = transpose(array([thickness_data[:,0],thickness_data[:,4],
28                                              thickness_data[:,5],thickness_data[:,9]]))
29     else:
30         thickness_data = genfromtxt(t_data, delimiter=',',skip_header=11)
31
32     # measurement_time is the time for the GISAXS measurements starting at t=0 seconds.
33     # the index of the vector signifies the measurement number
34     measurement_time = gisaxs_data[:,1] - gisaxs_data[0,1]
35
36     # at what index does thickness and gisaxs start?
37     thickness_start = t_index
38     gisaxs_start = g_index
39
40     # these are the wli thickness measurements after being synced
41     wli_thickness_time = thickness_data[thickness_start:-1,3] - thickness_data[
42         thickness_start,3]
43     wli_thickness = thickness_data[thickness_start:-1,1]
44
45     # initialize thickness as a function of measurement time
46     thickness = zeros((size(measurement_time),4))
47
48     # argmin finds the index of the minimum value in a vector
49     for i in arange(size(measurement_time)):
50         thickness_arg = argmin(abs(wli_thickness_time - measurement_time[i]))
51         thickness[i,1] = wli_thickness[int(thickness_arg)]
52         thickness[i,0] = i + gisaxs_start
53         thickness[i,2] = measurement_time[i]
54
55     # make a 4th column containing the samx value
56     samx_data = open(g_data,'r')
57     samx = []
58     for line in samx_data:
59         if line[:4] == "#P1 ":
```

```

59         if d1_2015:
60             samx.append(float(line.split(' ')[4]))
61         else:
62             samx.append(float(line.split(' ')[3]))
63
64 samx = asarray(samx)
65 samx_data.close()
66 thickness[:,3] = samx
67
68 return thickness
69
70 # takes a thickness data file as created in gisaxs_thickness and plots it
71 # shows both GISAXS image number and thickness on two seperate x-axes
72 # thanks to http://stackoverflow.com/questions/10514315/how-to-add-a-second-x-axis-in-
73 # matplotlib
74 # requires the data to be continuous (e.g. one thickness data file).
75 # Otherwise the GISAXS map x-axis is broken
76 def plot_gisaxs_thickness(thickness,index_phase=False,plot_phi=False, save_figure=False):
77
78     # tight axis
79     xlim(0,thickness[-1,2]/60)
80
81     # initial and max thickness found from data
82     d_initial = min(thickness[:,1])
83     d_max = max(thickness[:,1])
84
85     if plot_phi:
86         y_axis = d_initial/thickness[:,1]
87         ylabel("$\phi$")
88     else:
89         y_axis = thickness[:,1]
90         ylabel("Thickness [nm]")
91
92     plot(thickness[:,2]/60,y_axis,'.')
93     xlabel("Time [minutes]")
94
95     if index_phase:
96         y_axis_limit = ylim()
97         for i in index_phase:
98             plot((thickness[i,2]/60, thickness[i,2]/60), y_axis_limit, 'r-')
99             ylim(y_axis_limit)
100
101 disp('d_dry = ' + str(d_initial) + ' nm')
102 disp('d_max = ' + str(d_max) + ' nm')
103 disp('phi_min = ' + str(d_initial/d_max))
104
105 if save_figure:
106     savefig(save_figure + '.png', bbox_inches='tight', dpi=160)
107 else:
108     show()
109
110 # show a gisaxs image given a string dictating the directory, filename, experiment details
111 # , and data
112 # experiment is a vector with details of the experiment: [SD, pixel_size, db_x, db_y,
113 # alpha_i, wavelength]
114 # p_extent is the extent of the pixel area [x1, y1, x2, y2]
115 # imgtitle is the title of the plot
116 # colorlim defines the intensity limits of the plot (changes the colors of the plot quite
117 # a lot)
118 def show_gisaxs_image(dir, filename, experiment, p_extent=[0,0,-1,-1], imgtitle='', colorlim=(10.0,3e3), save_figure=False):
119     [x1, y1, x2, y2] = p_extent
120     im = imread(dir + filename)
121     im = flipud(im)
122     im = im[y1:y2,x1:x2]
123     im = flipud(im)
124
125     [qy1, qz1] = gisaxs_get_q(x1,y1,experiment)
126     [qy2, qz2] = gisaxs_get_q(x2,y2,experiment)
127
128     imgplot = imshow(im,norm=matplotlib.colors.LogNorm(),clim=colorlim,
129                      extent=[qy1,qy2,qz1,qz2], aspect='auto')
130     colorbar()
131
132     xlabel('q_y [nm$^{-1}$]')
133     ylabel('q_z [nm$^{-1}$]')
134     title(imgtitle)
135
136     if save_figure:
137         savefig(save_figure + '.png', bbox_inches='tight', dpi=160)
138     show()
139
140 # uses thickness data to return a string detailing the thickness and time for a specified

```

```

    GISAXS map
139 # well suited for making titles for show_gisaxs_image
140 # num: image number
141 # data: thickness data created by gisaxs_thickness()
142 # data_offset: the offset (index) that sets t=0
143 # state: a string describing the phase of the experiment (typically 'swelling' or 'drying
144 ')
144 def get_gisaxs_image_title(num, data, data_offset=0, state='experiment'):
145     index = where(data[:,0] == num)
146     time = (data[index,2] - data[data_offset,2]) / 60
147     samx = data[index,3]
148
149     title = str(num) + '.tif' + ' | ' + '%.1f' % data[index,1] + ' nm' \
150             + ' | ' + '%.1f' % time + ' min (' + str(state) + ') | samx=' + '%.1f' % samx
151
152     return title
153
154 # shows a 2d color plot from dpdak data
155 # data is 2d color plot data from a dpdak export (x-axis and data)
156 # axis is either "qz" or "qy" (this only changes the label on the plot)
157 def show_2d_colorplot(cp_data, th_data, axis='qz', colorlim=(10.0,5e2),samx_values='all'):
158     colorplot_data = genfromtxt(cp_data, skip_header=4)
159     num_inputs = size(colorplot_data,1)/2
160     x_axis = colorplot_data[:,0]
161     im = colorplot_data[:,num_inputs:-1]
162
163     #disp(size(im[0,:]))
164     #disp(size(th_data[:,3]))
165
166     if samx_values == 'all':
167         cond = ones(size(th_data[:,3]), dtype=bool)
168     else:
169         cond = zeros(size(th_data[:,3]), dtype=bool)
170         for i in samx_values:
171             cond = cond | (th_data[:,3] == i)
172
173     indices = transpose(where(cond))
174     indices = indices[:, -1, 0]
175     im = im[:, indices]
176
177     time_frames = size(im,1)
178
179     # Flip the data upside down. This is needed due to the way matrices are ordered.
180     imgplot = imshow(flipud(im), norm=matplotlib.colors.LogNorm(), clim=colorlim,
181                      extent=[1, time_frames, x_axis[0], x_axis[-1]], aspect='auto')
182     if axis == 'qz':
183         ylabel('q_z [nm^{(-1)}]')
184     if axis == 'qy':
185         ylabel('q_y [nm^{(-1)}]')
186
187     title('integration along ' + axis)
188     xlabel('time [frames]')
189     colorbar()
190     show()
191
192 # show phi and peakfit data on the same graph.
193 # when defining the model in DPDAK, the model has to be Lorenzian or Gaussian
194 # and be defined in the first line of the model box.
195 # That way, the first three coloums of peakfit_data are pos, height, fwhm
196 # To obtain the data from DPDAK use DB Export and ONLY select Peak Fit->fit_param
197 def show_phi_peakfit(data, peakfit_data, fwhm_cond=[0.01,0.05], samx_values='all', axis='
198     q_z',
199     peakfit_axis='fwhm', pos_cond=[0.32,0.40], save_figure=False):
200     peakfit = genfromtxt(peakfit_data, skip_header=4)
201
202     # conditions for fit
203     cond1 = peakfit[2,:] > fwhm_cond[0] #fwhm
204     cond2 = peakfit[2,:] < fwhm_cond[1] #fwhm
205
206     cond3 = peakfit[0,:] > pos_cond[0] # pos
207     cond4 = peakfit[0,:] < pos_cond[1] # pos
208
209     if samx_values=='all':
210         indices = where(cond1 & cond2 & cond3 & cond4)
211     else:
212         cond5 = zeros(size(data[:,3]), dtype=bool)
213         for i in samx_values:
214             cond5 = cond5 | (data[:,3] == i)
215         indices = where(cond1 & cond2 & cond3 & cond4 & cond5)
216
217     # draw everything
218     fig, ax1 = subplots()
219     t = transpose(data[indices,2]) / 60

```

```

220 fwhm = transpose(peakfit[2, indices])
221 pos = transpose(peakfit[0, indices])
222 height = transpose(peakfit[1, indices])
223
224 # output when we first see a peak that meet our conditions
225 disp('first point with condition fwhm in range ' + str(fwhm_cond) + ' at t=' + str(
226     data[indices[0][0], 2]/60)
227     + ', phi=' + str(min(data[:, 1])/data[indices[0][0], 1]))
228
229 if peakfit_axis == 'fwhm':
230     ax1.plot(t, fwhm, 'bo')
231     ax1.set_xlabel('time (minutes)')
232     if axis == 'q_z':
233         ax1.set_ylabel('w_z [nm^(-1)]', color='b')
234     if axis == 'q_y':
235         ax1.set_ylabel('w_y [nm^(-1)]', color='b')
236
237 if peakfit_axis == 'pos':
238     ax1.plot(t, pos, 'bo')
239     ax1.set_xlabel('time (minutes)')
240     ax1.set_ylabel(axis + '[nm^(-1)]', color='b')
241
242 if peakfit_axis == 'height':
243     ax1.plot(t, height, 'bo')
244     ax1.set_xlabel('time (minutes)')
245     ax1.set_ylabel('peak intensity (arb. units)', color='b')
246
247 if peakfit_axis == 'domain':
248     if axis == 'q_z':
249         disp('WARNING: Domain spacing should be found along q_y')
250
251     disp('hi')
252     ax1.plot(t, 2*pi/pos, 'bo')
253     ax1.set_xlabel('time (minutes)')
254     ax1.set_ylabel('domain spacing [nm]', color='b')
255
256 # tight x-axis
257 ax1.set_xlim(0, data[-1, 2]/60)
258
259 # Make the y-axis label and tick labels match the line color.
260 for tl in ax1.get_yticklabels():
261     tl.set_color('b')
262
263 ax2 = ax1.twinx()
264 t2 = data[:, 2]/60
265 phi = min(data[:, 1])/data[:, 1]
266 ax2.plot(t2, phi, 'g')
267 ax2.set_ylabel('$\phi$', color='g')
268 for tl in ax2.get_yticklabels():
269     tl.set_color('g')
270
271 if save_figure:
272     savefig(save_figure + '.png', bbox_inches='tight', dpi=160)
273 else:
274     show()
275
276 # get (qy, qz) at a pixel_x, pixel_y
277 # experiment vector contains details of experiment
278 # experiment = [SD, pixel_size, db_x, db_y, alpha_i, wavelength]
279 def gisaxs_get_q(pixel_x, pixel_y, experiment):
280     [SD, pixel_size, db_x, db_y, alpha_i, wavelength] = experiment
281
282     distance_z = (pixel_y-db_y)*pixel_size
283     alpha_f = arctan(distance_z/SD) - alpha_i
284     qz = 2*pi/wavelength*(sin(alpha_i) + sin(alpha_f))
285
286     distance_y = (pixel_x-db_x)*pixel_size
287     psi = arctan(distance_y/SD)
288     qy = 2*pi/wavelength*sin(psi)*cos(alpha_f)
289     return [qy, qz]
290
291 def load_gisaxs_data(filename):
292     datafile = load(filename)
293     data = datafile['arr_0']
294     datafile.close()
295     return data
296
297 *** Functions to use D1 data with GenX
298 reformat_data_for_genx() reformats the raw specuser data to a readable format for GenX
299 furthermore the x-axis is converted to q_z
300
301 display_genx_data simply takes the exports from GenX and displays them while
       outputting

```

```

302     fitting parameters to the console. In the Case of SLD it is converted to units of
303     Angstroms """
304 def display_genx_data(data_file, value_file, sld_file):
305     # some values we need
306     f_C = 6.01131
307     f_H = 0.999979
308     f_O = 8.03236
309     f_Si = 14.1795
310     r_e = 2.81794033e-5
311
312     data = genfromtxt(data_file)
313     values = genfromtxt(value_file, delimiter='\t')
314     sld = genfromtxt(sld_file)
315     x = data[:,0]*10
316     I = data[:,2]
317     Isim = data[:,1]
318
319     # plot reflectivity and fit
320     figure(figsize=(8,6), dpi=160)
321     semilogy(x,I, 'o', label='data', markersize=10)
322     semilogy(x,Isim, 'r-', label='model', linewidth=2)
323     xlabel('q_z [nm^{-1}]', fontsize='x-large')
324     ylabel('R', fontsize='x-large')
325     legend(loc='upper right', fontsize='x-large')
326     autoscale(enable=True, axis=u'both', tight=True)
327     savefig(data_file + '_ref.png', bbox_inches='tight', dpi=160)
328     show()
329
330     # plot sld
331     figure(figsize=(8,6), dpi=160)
332     plot(sld[:,0]*0.1,sld[:,1], linewidth=2)
333     xlabel('z [nm]', fontsize='x-large')
334     ylabel('SLD [$r_e/\text{AA}^3$]', fontsize='x-large')
335     autoscale(enable=True, axis=u'both', tight=True)
336     savefig(data_file + '_sld.png', bbox_inches='tight', dpi=160)
337     show()
338
339     f_polymer = 6*f_C + 7*f_H
340     f_SiOx = 1*f_Si + 2*f_O
341     polymer_thickness = values[1,1]
342     polymer_sld = values[2,1]*f_polymer*r_e
343     polymer_sigma = values[3,1]
344     siox_thickness = values[4,1]
345     siox_sld = values[5,1]*f_SiOx*r_e
346     siox_sigma = values[6,1]
347     si_sld = values[7,1]*f_Si*r_e
348
349     disp('polymer thickness: ' + str(polymer_thickness) + ' AA')
350     disp('polymer SLD: ' + str(polymer_sld) + ' AA^{(-2)}')
351     disp('polymer roughness: ' + str(polymer_sigma))
352     disp('SiOx thickness: ' + str(siox_thickness) + ' AA')
353     disp('SiOx SLD: ' + str(siox_sld) + ' AA^{(-2)}')
354     disp('SiOx roughness: ' + str(siox_sigma))
355     disp('Si SLD: ' + str(si_sld) + ' AA^{(-2)})')
356
357     # if we want to compare sld profiles of different measurements
358     return sld
359
360 def reformat_data_for_genx(datafile, Iback, Idirect, seconds, wavelength):
361     c4r1 = genfromtxt(datafile)
362     angle = c4r1[:,0]
363     Imon = c4r1[:,4]/seconds
364     Idet = c4r1[:,5]/seconds
365     q_z = 4*pi*sin(angle*degree)/wavelength
366
367     R = (Idet/Imon - Iback)/(Idirect)
368     #semilogy(q_z,R)
369     #xlabel('angle (degrees)')
370     #ylabel('intensity (arb. u.)')
371
372     savetxt(datafile + '.out', transpose([q_z, R]))

```

## D1Ba.py

`D1Ba.py` is a header file for BornAgain containing some default settings that work well for GISAXS at D1. Furthermore, a way to plot the simulation results as a function of  $q_y$  and  $q_z$  has been implemented. Requires a working BornAgain[11] installation to work.

## D1Ba.py

```

1 import numpy
2 import matplotlib
3 import pylab
4 import scipy.special
5 from bornagain import *
6
7 # homemade header for bornagain.
8 # running and plotting the simulation has been generalized somewhat
9
10 # choosing what to export
11 __all__ = ["GISAXSExperiment", "plot_result", "get_simulation", "run_simulation"]
12
13 # class containing the details of the experiment
14 # the function setQLimits() finds the limits in q-space based on wavelength and phi, alpha
15 # limits
16 # defaults are values from D1
17 class GISAXSExperiment:
18     wavelength = 1.16*angstrom
19     alpha_i = 0.14*degree
20     phi_i = 0.0*degree
21     phi_min, phi_max = -0.65*degree, 0.65*degree
22     alpha_min, alpha_max = 0.0*degree, 0.8*degree
23     binx = 200
24     biny = 200
25
26     mc = False
27     mc_points = 50
28
29     multithreading = True
30
31     detector_resolution = False
32
33     def __init__(self):
34         self.setQLimits()
35
36     def setQLimits(self):
37         self.qy_min = 2*numpy.pi/self.wavelength*(numpy.sin(self.phi_min)*numpy.cos(self.
38             alpha_min))
39         self.qy_max = 2*numpy.pi/self.wavelength*(numpy.sin(self.phi_max)*numpy.cos(self.
40             alpha_max))
41         self.qz_min = 2*numpy.pi/self.wavelength*(numpy.sin(self.alpha_i) + numpy.sin(self.
42             alpha_min))
43         self.qz_max = 2*numpy.pi/self.wavelength*(numpy.sin(self.alpha_i) + numpy.sin(self.
44             alpha_max))
45
46     # function to plot data
47     # exp is a GISAXSExperiment class
48     # result is the result from run_simulation
49     # units is either "degrees" or "qspace"
50     def plot_result(result, exp, units, save_figure=False):
51         if save_figure:
52             pylab.style.use('presentation.mplstyle')
53
54         if units == "degrees":
55             im = pylab.imshow(numpy.rot90(result, 1), norm=matplotlib.colors.LogNorm(),
56                               extent=[exp.phi_min/degree, exp.phi_max/degree, exp.alpha_min/
57                                     degree, exp.alpha_max/degree],
58                               aspect='auto')
59             cb = pylab.colorbar(im)
60             cb.set_label(r'Intensity (arb. u.)')
61             pylab.xlabel(r'$\phi_f$')
62             pylab.ylabel(r'$\alpha_f$')
63
64         if units == "qspace":
65             # get the limits in q-space
66             exp.setQLimits()
67             im = pylab.imshow(numpy.rot90(result, 1), norm=matplotlib.colors.LogNorm(),
68                               extent=[exp.qy_min, exp.qy_max, exp.qz_min, exp.qz_max],
69                               aspect='auto')
70             cb = pylab.colorbar(im)
71             cb.set_label(r'Intensity (arb. u.)')
72             pylab.xlabel(r'$q_y$ [nm$^{-1}$]')
73             pylab.ylabel(r'$q_z$ [nm$^{-1}$]')
74
75         if save_figure:
76             pylab.savefig(save_figure + '.png', bbox_inches='tight', dpi=160)
77         else:
78             pylab.show()
79
80     # getting the simulation
81     def get_simulation(exp):
82         simulation = GISASSimulation()
83
84

```

```

77 # instrumentation
78 simulation.setDetectorParameters(exp.binx, exp.phi_min, exp.phi_max, exp.biny, exp.
79     alpha_min, exp.alpha_max)
80 simulation.setBeamParameters(exp.wavelength, exp.alpha_i, exp.phi_i)
81
82 # monte carlo simulation
83 if exp.mc:
84     sim_pars = SimulationParameters()
85     sim_pars.m_mc_integration = True
86     sim_pars.m_mc_points = exp.mc_points
87     simulation.setSimulationParameters(sim_pars)
88
89 # multithreading must be disabled for custom form factors
90 if not exp.multithreading:
91     thread_info = ThreadInfo()
92     thread_info.n_threads = -1
93     simulation.setThreadInfo(thread_info)
94
95 return simulation
96
97 # running the simulation
98 # sample is the result of GISAXSSample.getSample
99 # exp is a GISAXSExperiment class
100 def run_simulation(sample, exp):
101     simulation = get_simulation(exp)
102
103     if exp.detector_resolution:
104         resolution_function = ResolutionFunction2DGaussian(exp.detector_resolution, exp.
105             detector_resolution)
106         simulation.setDetectorResolutionFunction(resolution_function)
107
108     simulation.setSample(sample)
109     simulation.runSimulation()
109     result = simulation.getIntensityData()
109
109 return result

```

## cylinders.py

`cylinders.py` contain the code for simulations carried out in section 2.3. Requires a working BornAgain[11] installation to work.

cylinders.py

```

1 # vertical cylinders in hexagonal lattice
2
3 import numpy
4 import matplotlib
5 import pylab
6 from bornagain import *
7 from DIBa import *
8
9 # set sample parameters
10 Si = 6.08e-6
11 PS = 2.17e-6
12 PB = 1.88e-6
13
14 # optional: contrast
15 contrast = 0.1
16 PS = contrast*PS
17
18 # defining materials
19 m_ambience = HomogeneousMaterial("Air", 0.0, 0.0)
20 m_substrate = HomogeneousMaterial("Substrate", Si, 0.0)
21 m_particle = HomogeneousMaterial("Particle", PS, 0.0)
22 m_matrix = HomogeneousMaterial("Matrix", PB, 0.0)
23
24 def get_sample_vertical(thickness=250.0*nanometer, radius=15.0*nanometer,
25                         volume_fraction=0.7, order_parameter=0.02, slices=1,
26                         interference=True):
27
28     # height of one slice
29     height = thickness
30
31     # determine spacing in terms of volume fraction
32     spacing = numpy.sqrt(2*numpy.pi/volume_fraction)*radius/(3.0**((1.0/4.0)))
33     numpy disp('HEX spacing: ' + str(spacing))
34
35     # define coherence lengths through order parameter
36     clx = order_parameter*spacing
37     cyl = clx

```

```

38     ff = FormFactorCylinder(radius, height/slices)
39     composition = ParticleComposition()
40
41     for i in numpy.arange(0,slices):
42         composition.addParticle(Particle(m_particle, ff), kvector_t(0,0,i*height/slices))
43
44     particle_layout = ParticleLayout()
45     particle_layout.addParticle(composition, 1.0, kvector_t(0.0, 0.0, -height))
46
47     if interference:
48         if interference == 'square':
49             interference_function = InterferenceFunction2DParaCrystal.createSquare(spacing)
50         if interference == 'hex':
51             interference_function = InterferenceFunction2DParaCrystal.createHexagonal(
52                 spacing)
53
54     pdf = FTDistribution2DGauss(clx, cly)
55     interference_function.setProbabilityDistributions(pdf, pdf)
56     interference_function.setIntegrationOverXi(True)
57     particle_layout.addInterferenceFunction(interference_function)
58
59     air_layer = Layer(m_ambience)
60     polymer_layer = Layer(m_matrix, height)
61     polymer_layer.setLayout(particle_layout)
62     substrate_layer = Layer(m_substrate)
63
64     multi_layer = MultiLayer()
65     multi_layer.addLayer(air_layer)
66     multi_layer.addLayer(polymer_layer)
67     multi_layer.addLayer(substrate_layer)
68
69     return multi_layer
70
71 def get_sample_homogeneous(thickness=250.0*nanometer, sigma=5*nanometer, hurst=0.3):
72     air_layer = Layer(m_ambience)
73     polymer_layer = Layer(m_matrix, thickness)
74     substrate_layer = Layer(m_substrate)
75
76     roughness = LayerRoughness()
77     roughness.setSigma(sigma)
78     roughness.setHurstParameter(hurst)
79     roughness.setLatteralCorrLength(sigma)
80
81     multi_layer = MultiLayer()
82     multi_layer.addLayer(air_layer)
83     multi_layer.addLayerWithTopRoughness(polymer_layer, roughness)
84     multi_layer.addLayer(substrate_layer)
85
86     return multi_layer
87
88 def get_sample_horizontal(radius=15.0*nanometer, volume_fraction=0.7, order_parameter=
89     =0.05,
90     layers=10,length=200.0*nanometer, interference=True):
91
92     # side length t and smallest with a of hexagon
93     t = numpy.sqrt(2*numpy.pi/volume_fraction)*radius/(3.0**((1.0/4.0)))
94     a = numpy.sqrt(3.0)*t/2.0
95
96     clx = order_parameter*t
97     cly = order_parameter*length
98
99     cylinder_ff = FormFactorCylinder(radius, length)
100    cylinder = Particle(m_particle, cylinder_ff)
101
102    composition = ParticleComposition()
103    position = kvector_t(0,0,0)
104    composition.addParticle(cylinder, position)
105
106    thickness = a+2*radius
107
108    particle_layout = ParticleLayout()
109    rotation = RotationX(90.0*degree)
110
111    particle_layout.addParticle(composition, 1.0, kvector_t(0.0, 0.0, -thickness+a/2),
112        rotation)
113    if interference:
114        interference_function = InterferenceFunction2DParaCrystal(t, length, 90.0*degree,
115            0.0*degree)
116        pdf_x = FTDistribution2DGauss(clx, cly)
117        pdf_y = FTDistribution2DGauss(clx, cly)
118        interference_function.setProbabilityDistributions(pdf_x, pdf_y)
119        interference_function.setIntegrationOverXi(True)

```

```

117     interference_function.setDomainSizes(200.0*micrometer, 200.0*micrometer)
118     particle_layout.addInterferenceFunction(interference_function)
119
120     air_layer = Layer(m_ambience)
121     polymer_layer = Layer(m_matrix, thickness)
122     polymer_layer.addLayout(particle_layout)
123     substrate_layer = Layer(m_substrate)
124
125     multi_layer = MultiLayer()
126     multi_layer.addLayer(air_layer)
127     for i in numpy.arange(0, layers):
128         multi_layer.addLayer(polymer_layer)
129
130     multi_layer.addLayer(substrate_layer)
131
132     numpy.disp('HEX spacing: ' + str(t) + ' nm')
133     numpy.disp('Film thickness (' + str(layers) + ', layers): ' + str(thickness) + ' nm')
134     numpy.disp('Horizontal spacing: ' + str(a) + ' nm')
135
136     return multi_layer
137
138 if __name__ == '__main__':
139     exp = GISAXSExperiment()
140
141     #exp.phi_min, exp.phi_max = 0.2*degree, 0.4*degree
142     #exp.alpha_min, exp.alpha_max = 0.0*degree, 0.6*degree
143
144     exp.mc = False
145     exp.mc_points = 50
146
147     exp.detector_resolution = False
148
149     exp.binx = 200
150     exp.biny = exp.binx
151
152     sample_type = 'horizontal'
153
154     if sample_type == 'vertical':
155         sample = get_sample_vertical(thickness=200.0*nanometer, radius=15.0*nanometer,
156                                     volume_fraction=0.7, order_parameter=0.05, slices=1,
157                                     interference='hex')
158
159     if sample_type == 'horizontal':
160         sample = get_sample_horizontal(radius=15.0*nanometer, volume_fraction=0.7,
161                                         order_parameter=0.02,
162                                         layers=5, length=100.0*nanometer, interference=True)
163
164     if sample_type == 'homogeneous':
165         sample = get_sample_homogeneous(thickness=200.0*nanometer, sigma=5.0*nanometer)
166
167     sample.printParameters()
168
169     output = run_simulation(sample, exp)
170     result = output.getArray() + 1
171     plot_result(result, exp, "qspace")

```



## Bibliography

- [1] J. Als-Nielsen and D. McMorrow. *Elements of Modern X-ray Physics*. Wiley, 2011. ISBN 9781119970156.
- [2] Frank S Bates and Glenn H Fredrickson. Block copolymer thermodynamics: theory and experiment. *Annual Review of Physical Chemistry*, 41(1):525–557, 1990.
- [3] Frank S Bates, Marc A Hillmyer, Timothy P Lodge, Christopher M Bates, Kris T Delaney, and Glenn H Fredrickson. Multiblock polymers: panacea or pandoras box? *Science*, 336(6080):434–440, 2012.
- [4] Gunthard Benecke, Wolfgang Wagermaier, Chenghao Li, Matthias Schwartzkopf, Gero Flucke, Rebecca Hoerth, Ivo Zizak, Manfred Burghammer, Ezzeldin Metwalli, Peter Müller-Buschbaum, et al. A customizable software for fast reduction and analysis of large x-ray scattering data sets: applications of the new dpdak package to small-angle x-ray scattering and grazing-incidence small-angle x-ray scattering. *Journal of applied crystallography*, 47(5):1797–1803, 2014.
- [5] Matts Björck and Gabriella Andersson. Genx: an extensible x-ray reflectivity refinement program utilizing differential evolution. *Journal of Applied Crystallography*, 40(6):1174–1178, 2007.
- [6] Johannes Brandrup, Edmund H Immergut, Eric A Grulke, Akihiro Abe, and Daniel R Bloch. *Polymer handbook*, volume 89. Wiley New York, 1999.
- [7] Michelle A Chavis, Detlef-M Smilgies, Ulrich B Wiesner, and Christopher K Ober. Widely tunable morphologies in block copolymer thin films through solvent vapor annealing using mixtures of selective solvents. *Advanced Functional Materials*, 25(20):3057–3065, 2015.
- [8] Slim T Chourou, Abhinav Sarje, Xiaoye S Li, Elaine R Chan, and Alexander Hexemer. Hipgisaxs: a high-performance computing code for simulating grazing-incidence x-ray scattering data. *Journal of Applied Crystallography*, 46(6):1781–1795, 2013.
- [9] Cornell High Energy Synchrotron Source. Chess. <http://www.chess.cornell.edu/>, 2015. Website accessed on 09-28-2015.
- [10] Zhenyu Di, Dorthe Posselt, Detlef-M Smilgies, and Christine M Papadakis. Structural rearrangements in a lamellar diblock copolymer thin film during treatment with saturated solvent vapor. *Macromolecules*, 43(1):418–427, 2009.
- [11] C. Durniak, M. Ganeva, G. Pospelov, Van Herck W., and Wuttke J. Bornagain - software for simulating and fitting x-ray and neutron small-angle scattering at grazing incidence. <http://www.bornagainproject.org/>, 2015.
- [12] E Bhoje Gowd, Tadanori Koga, Maya K Endoh, Kamlesh Kumar, and Manfred Stamm. Pathways of cylindrical orientations in ps-b-p4vp diblock copolymer thin films upon solvent vapor annealing. *Soft matter*, 10(39):7753–7761, 2014.

- [13] David Jeffrey Griffiths and Reed College. *Introduction to electrodynamics*, volume 3. Prentice Hall Upper Saddle River, NJ, 1999.
- [14] Xiaodan Gu, Ilja Gunkel, Alexander Hexemer, Weiyin Gu, and Thomas P Russell. An in situ grazing incidence x-ray scattering study of block copolymer thin films during solvent vapor annealing. *Advanced Materials*, 26(2):273–281, 2014.
- [15] David B Hall, Patrick Underhill, and John M Torkelson. Spin coating of thin and ultrathin polymer films. *Polymer Engineering and Science*, 38(12):2039–2045, 1998.
- [16] Ian W Hamley et al. *Developments in block copolymer science and technology*. Wiley Online Library, 2004.
- [17] Eugene Helfand and Yukiko Tagami. Theory of the interface between immiscible polymers. ii. *The Journal of Chemical Physics*, 56(7):3592–3601, 1972.
- [18] Burton L Henke. Atomic scattering factors. [http://henke.lbl.gov/optical\\_constants/asf.html](http://henke.lbl.gov/optical_constants/asf.html), 1993. Website accessed on 09-12-2015.
- [19] Burton L Henke, Eric M Gullikson, and John C Davis. X-ray interactions: photoabsorption, scattering, transmission, and reflection at  $e = 50\text{--}30,000 \text{ ev}$ ,  $z = 1\text{--}92$ . *Atomic data and nuclear data tables*, 54(2):181–342, 1993.
- [20] Alexander Hexemer and Peter Müller-Buschbaum. Advanced grazing-incidence techniques for modern soft-matter materials analysis. *IUCrJ*, 2(1):106–125, 2015.
- [21] AM Hindeleh and R Hosemann. Paracrystals representing the physical state of matter. *Journal of Physics C: Solid State Physics*, 21(23):4155, 1988.
- [22] Zhang Jiang, Dong Ryeol Lee, Suresh Narayanan, Jin Wang, and Sunil K Sinha. Waveguide-enhanced grazing-incidence small-angle x-ray scattering of buried nanostructures in thin films. *Physical Review B*, 84(7):075440, 2011.
- [23] Remi Lazzari. Isgisaxs: a program for grazing-incidence small-angle x-ray scattering analysis of supported islands. *Journal of Applied Crystallography*, 35(4):406–421, 2002.
- [24] Byeongdu Lee, Insun Park, Jinhwan Yoon, Soojin Park, Jehan Kim, Kwang-Woo Kim, Taihyun Chang, and Moonhor Ree. Structural analysis of block copolymer thin films with grazing incidence small-angle x-ray scattering. *Macromolecules*, 38(10):4311–4323, 2005.
- [25] Yuan Li, Xiaochu Wang, Isaac C Sanchez, Keith P Johnston, and Peter F Green. Ordering in asymmetric block copolymer films by a compressible fluid. *The Journal of Physical Chemistry B*, 111(1):16–25, 2007.
- [26] MW Matsen and Frank S Bates. Unifying weak-and strong-segregation block copolymer theories. *Macromolecules*, 29(4):1091–1098, 1996.
- [27] Dr. Andreas Meyer. <http://gisaxs.de/theory.html>, 2011. Website accessed on 09-07-2015.
- [28] P Müller-Buschbaum. A basic introduction to grazing incidence small-angle x-ray scattering. In *Applications of Synchrotron Light to Scattering and Diffraction in Materials and Life Sciences*, pages 61–89. Springer, 2009.
- [29] Christine M Papadakis, Kristoffer Almdal, Kell Mortensen, and Dorthe Posselt. A small-angle scattering study of the bulk structure of a symmetric diblock copolymer system. *Journal de Physique II*, 7(12):1829–1854, 1997.
- [30] CM Papadakis, C Darko, Z Di, K Troll, E Metwalli, A Timmann, G Reiter, and S Förster. Surface-induced breakout crystallization in cylinder-forming p (ib-eo) diblock copolymer thin films. *The European Physical Journal E*, 34(1):1–8, 2011.

- 
- [31] Lyman G Parratt. Surface studies of solids by total reflection of x-rays. *Physical review*, 95(2):359, 1954.
  - [32] Polymer Source. Sample p376-sbd. <http://polymersource.com/>, 2015. Website accessed on 09-24-2015.
  - [33] Igor I Potemkin. Lamellar orientation in thin, supported diblock copolymer films: strong segregation theory. *Macromolecules*, 37(9):3505–3509, 2004.
  - [34] Gilles Renaud, Rémi Lazzari, and Frédéric Leroy. Probing surface and interface morphology with grazing incidence small angle x-ray scattering. *Surface Science Reports*, 64(8):255–380, 2009.
  - [35] Rachel A Segalman. Patterning with block copolymer thin films. *Materials Science and Engineering: R: Reports*, 48(6):191–226, 2005.
  - [36] Christophe Sinturel, Marylène Vayer, Michael Morris, and Marc A Hillmyer. Solvent vapor annealing of block polymer thin films. *Macromolecules*, 46(14):5399–5415, 2013.
  - [37] Detlef-M Smilgies. Instructions for xr at the d1 beamline. <http://staff.chess.cornell.edu/~smilgies/D-lineNotes/XR-at-D1.html>, 2015. Website accessed on 09-29-2015.
  - [38] Paul A Tipler and Gene Mosca. *Physics for scientists and engineers*. Macmillan, 2007.
  - [39] Metin Tolan. *X-ray scattering from soft-matter thin films*. Springer, 1999.
  - [40] A Van Der Lee, F Salah, and B Harzallah. A comparison of modern data analysis methods for x-ray and neutron specular reflectivity data. *Journal of Applied Crystallography*, 40(5):820–833, 2007.
  - [41] George H Vineyard. Grazing-incidence diffraction and the distorted-wave approximation for the study of surfaces. *Physical Review B*, 26(8):4146, 1982.
  - [42] Y Yoneda. Anomalous surface reflection of x rays. *Physical Review*, 131(5):2010, 1963.
  - [43] Jinhwan Yoon, Seung Yun Yang, Byeongdu Lee, Wonchul Joo, Kyuyoung Heo, Jin Kon Kim, and Moonhor Ree. Nondestructive quantitative synchrotron grazing incidence x-ray scattering analysis of cylindrical nanostructures in supported thin films. *Journal of Applied Crystallography*, 40(2):305–312, 2007.
  - [44] Jianqi Zhang, Dorthe Posselt, Detlef-M Smilgies, Jan Perlich, Konstantinos Kyriakos, Sebastian Jakusch, and Christine M Papadakis. Lamellar diblock copolymer thin films during solvent vapor annealing studied by gisaxs: Different behavior of parallel and perpendicular lamellae. *Macromolecules*, 47(16):5711–5718, 2014.